X-ray multiple-beam (n-baem) dynamical diffraction theories, numerical methods to solve them and experimental verification by using the synchrotron X-rays *

Kouhei OKITSU

Nano-Engineering Research Center, Institute of Engineering Innovation, Graduate School of Engineering, The University of Tokyo, 2-11-16 Yayoi, Bunkyo-ku, Tokyo 113-8656, Japan. Correspondence e-mail: tkokitsu@g.ecc.u-tokyo.ac.jp

September 10, 2024

Abstract

Behavior of X-rays diffracted in a perfect or quasi-perfect crystal can be described by the dynamical theory of X-ray diffraction. Study on the two-beam cases in which only transmitted and one reflected X-ray beams are strong has a history of one hundred years. However, the population of researchers who study on the multiple-beam cases (n-beam cases) in which more than two beams are simultaneously strong is small. The present author has derived the Takagi-Taupin (T-T) dynamical theory that can be applied to the n-beam cases, coded the computer programs to solve it and experimentally verified them by using the synchrotron X-rays. The equivalence between the Ewald-Laue (E-L) and the T-T dynamical theories described by the Fourier transform also for the n-beam cases is explicitly verified in the present paper. Further, the methods of the computer simulations and the experiments are also described.

Furthermore, a hypothesis concerning the too large values of R-factor in protein crystallography is also described. This might be extremely important in protein crystallography in the future.

Keywords: X-ray diffraction, dynamical diffraction theory, multiple-beam diffraction, n-beam diffraction, Takagi-Taupin equation, silicon crystal, diamond crystal, X-ray phase retarder, computer simulation, synchrotron radiation, protein crystallography, phase problem

1 Introduction

The theory that describes the behavior of X-rays diffracted in a perfect or quasi-perfect crystal is called as the dynamical theory. Just after the discovery of the X-ray diffraction by von. Laue, basic theories were given by Darwin [1, 2] and by Ewald [3]. The most widely known

*The present manuscript has been translated to submitted to arXiv from a review article published in Journal of the Japanese Society for Synchrotron Radiation Research (2020) **33** 61-80 [in Japanese].

dynamical theory is the Ewald-Laue (E-L) theory that has been derived by applying the two-beam approximation to the fundamental equation given by von. Laue [4]. There are several textbooks that describe the dynamical theory [5–8].

However, the Takagi-Taupin (T-T) equation that has been derived by Takagi [9–12] was accepted as another form of the dynamical theory. It can deal with the X-ray wave field in a distorted crystal. Various images of the crystal defects were computer-simulated based on the T-T equation [13, 14].

Incidentally, it can easily be understood that n reciprocal lattice nodes ($n \geq 3$) can exist on the surface of the Ewald sphere by rotating the crystal around the axis of $\overrightarrow{\mathrm{H_0H_1}}$. Here, $\mathrm{H_0}$ is the origin of the reciprocal space and $\mathrm{H_1}$ is the reciprocal lattice node that causes the $\overrightarrow{\mathrm{H_0H_1}}$ reflection. X-ray intensity measurement taken by rotating the $\overrightarrow{\mathrm{H_0H_1}}$ axis is called as the Renninger scan [15].

While silicon, diamond and/or germanium crystals are usually used as the monochromator in the energy scan of X-ray spectroscopy, discontinuities of the X-ray intensity are frequently found and referred to as glitches. When scanning the photon energy of X-rays by rotating the monochromator crystal, the radius of the Ewald sphere changes. Then, a third reciprocal lattice node other than the origin of the reciprocal space $\mathrm{H_0}$ and reciprocal lattice node $\mathrm{H_1}$ giving the primary reflection causes the glitch when it exists on the surface of the Ewald sphere.

Let refer to the case that n-reciprocal lattice nodes $\mathrm{H_0}$, $\mathrm{H_1}$, $\mathrm{H_2}$, $\cdots$, $\mathrm{H_{n-1}}$ exist on the surfaces of the Ewald sphere as the n-beam cases. The E-L two-beam dynamical diffraction theory was extended such as to deal with the n-beam cases in 1965-1968 [16–21]. The numerical method to solve the theory was given by Colella in 1974 [22].

However, the extension of the T-T equation was delayed for many years due to the complexity when dealing with the polarization effect of X-rays. The three-beam T-T equation that neglected the polarization effect was given by Thorkildsen in 1987 [23]. The T-T equation that takes into account the polarization factor was for the first time given by Larsen and Thorkildsen in 1998 [24]. The present author reported the T-T equation extended to the n-beam cases for $n \in \{3, 4, 6, 8, 12\}$ in 2003 [25]. The numerical method to solve it and experimental verification by using the synchrotron radiation was given by the present author and coauthors for a six-beam case [26–28]. The computer-simulated and experimentally obtained results to be compared with each other for the n-beam cases were reported for $n \in \{3, 4, 5, 6, 8, 12\}$ in 2012 by Okitsu, Imai and Yoda [29]. The excellent agreements were found between the computer-simulated and the experimentally obtained pinhole topographs.

Between the E-L and the T-T dynamical theories, there is a simple relation described by the Fourier transform that has been implicitly recognized but has been explicitly described for the first time in 2012 [29]. It can be recognized that this delayed the extension to the n-beam cases of the T-T equation in comarison with the E-L dynamical theory.

In the present paper, the n-beam E-L theory is derived from Laue's fundamental equation of the dynamical theory [4] at first. Then, the n-beam T-T equation is derived by Fourier-transforming the n-beam E-L theory. The equivalence between the n-beam E-L and T-T dynamical theories is explicitly described also for an arbitrary number of n.

The n-beam dynamical diffraction phenomena of X-rays can be described by both the T-T and E-L theories and be numerically solved. The numerical methods to solve these theories have advantages and disadvantages when compared with each other. The present author considers that they should be used depending to the purpose with this recognition.

Authier's book describing the dynamical theory of X-ray diffraction [8] is recognized to be the most widely read textbook that has over 500 pages. However, it has only 24 pages for description

on the n-beam diffraction. In Pinsker's book [7], descriptions concerning the n-beam E-L theory are found. These have been revied by Weckert and Hümmer [30, 31] and Colella [32, 33].

2 Derivation of the Ewald-Laue (E-L) n-beam dynamical theory

The following equation is the fundamental equation of the dynamical theory [4]:

$$\frac{k_i^2 - K^2}{k_i^2}\boldsymbol{\mathcal{D}}_i = \sum_j \chi_{h_i - h_j} \left[\boldsymbol{\mathcal{D}}_j\right]_{\perp \mathbf{k}_i}. \tag{1}$$

Here, k_i is the wavenumber of the ith numbered Bloch wave whose wavevector is $\mathbf{k}_i$ $(= \mathbf{k}_0 + \mathbf{h}_i)$ of the ith numbered Bloch wave. $\mathbf{k}_0$ is the forward-diffracted X-ray beam in the crystal. $\mathbf{h}_i$ is the scattering vector. $K(= 1/\lambda)$ is the the wavenumber of the incident X-rays in vacuum where λ is the wavelength of them. $\boldsymbol{\mathcal{D}}_i$ and $\boldsymbol{\mathcal{D}}_j$ are amplitude vectors of the ith and jth numbered Bloch waves. $\sum_j$ is the infinite summation for j. $\chi_{h_i - h_j}$ is the Fourier coefficient of the electric susceptibility. $[\boldsymbol{\mathcal{D}}_j]_{\perp \mathbf{k}_i}$ is the vector component of $\boldsymbol{\mathcal{D}}_j$ perpendicular to $\mathbf{k}_i$.

By applying the approximation of $k_i + K \approx 2k_i$ to (1), the following equation can be obtained:

$$\xi_i \boldsymbol{\mathcal{D}}_i = \frac{K}{2} \sum_j \chi_{h_i - h_j} \left[\boldsymbol{\mathcal{D}}_j\right]_{\perp \mathbf{k}_i}, \tag{2}$$
$$\text{where} \quad \xi_i = k_i - K.$$

The electric displacement vectors $\boldsymbol{\mathcal{D}}_i$ and $\boldsymbol{\mathcal{D}}_j$ can be reperesented as linear combinations of the scalar electric displacements as follows:

$$\boldsymbol{\mathcal{D}}_i = \mathcal{D}_i^{(0)} \mathbf{e}_i^{(0)} + \mathcal{D}_i^{(1)} \mathbf{e}_i^{(1)}, \tag{3a}$$
$$\boldsymbol{\mathcal{D}}_j = \mathcal{D}_j^{(0)} \mathbf{e}_j^{(0)} + \mathcal{D}_j^{(1)} \mathbf{e}_j^{(1)}. \tag{3b}$$

When $\mathbf{s}_i$ is a unit vector in the direction of $\mathbf{k}_i$ and then $\mathbf{e}_i^{(0)}$ and $\mathbf{e}_i^{(1)}$ are defined such that $\mathbf{s}_i$, $\mathbf{e}_i^{(0)}$ and $\mathbf{e}_i^{(1)}$ construct a right-handed orthogonal system in this order. $\mathbf{s}_j$, $\mathbf{e}_j^{(0)}$ and $\mathbf{e}_j^{(1)}$ are defined in the same way.

With regard to the following description, Fig. 1 should be referred. When considering the number of n for cubic crystals with the highest symmetry, the number of reciprocal lattice nodes n that can simultaneously exist on the surface of the Ewald sphere, is restricted to be 3, 4, 5, 6, 8 and 12 by applying the approximation that the distances of the reciprocal lattice nodes other than n reciprocal lattice nodes to be taken into account, are sufficiently far from the surface of the Ewald sphere. The Laue point La_0 is the point whose distance from the reciprocal lattice nodes H_i $(i \in \{0, 1, \cdots, n-1\})$ is K $(= 1/\lambda)$. λ is the wavelength of the X-rays in vacuum. Pl_i is a plane surface that approximates the sphere whose radius is K and center is H_i. Only Pl_0 and Pl_3 are drawn in Fig. 1. The Laue point is darely symbolized as La_0 such that the theories can be extended for the cases that $|\overrightarrow{\mathrm{La}_0\mathrm{H}_i}|$ is not exactly equal K.

P_1 is the point on Pl_0 that is the start point of the wavevector of the incident X-rays whose end point is H_0. The polarization factors C and S are defined as follows,

$$\mathbf{e}_j^{(m)} = S_{i,j}^{(m)} \mathbf{s}_i + C_{i,j}^{(0,m)} \mathbf{e}_i^{(0)} + C_{i,j}^{(1,m)} \mathbf{e}_i^{(1)}. \tag{4}$$

Therefore,

$$S_{i,j}^{(m)} = \mathbf{s}_i \cdot \mathbf{e}_j^{(m)}, \tag{5a}$$

$$C_{i,j}^{(0,m)} = \mathbf{e}_i^{(0)} \cdot \mathbf{e}_j^{(m)}, \tag{5b}$$

$$C_{i,j}^{(1,m)} = \mathbf{e}_i^{(1)} \cdot \mathbf{e}_j^{(m)}. \tag{5c}$$

By substituting (3a) and (3b) into the left and right sides of (2), respectively, the following equations can be obtained:

$$\xi_i\big(\mathcal{D}_i^{(0)}\mathbf{e}_i^{(0)} + \mathcal{D}_i^{(1)}\mathbf{e}_i^{(1)}\big) = \frac{K}{2}\sum_{j=0}^{n-1}\chi_{h_i-h_j}\big[\mathcal{D}_j^{(0)}\mathbf{e}_j^{(0)} + \mathcal{D}_j^{(1)}\mathbf{e}_j^{(1)}\big]_{\perp\mathbf{k}_i}. \tag{6}$$

By substituting (4) into the right side of (6) and comparing the terms of $\mathbf{e}_i^{(l)}$,

$$\xi_i\mathcal{D}_i^{(l)} = \frac{K}{2}\sum_{j=0}^{n-1}\chi_{h_i-h_j}\sum_{m=0}^{1}C_{i,j}^{(l,m)}\mathcal{D}_j^{(m)}. \tag{7}$$

$\overrightarrow{\mathrm{P}_1'\mathrm{P}_1}$ is parallel to the downward surface normal $\mathbf{n}_z$ of the crystal and described as follows:

$$\overrightarrow{\mathrm{P}_1'\mathrm{P}_1} = \xi\mathbf{n}_z. \tag{8}$$

$\beta^{(0)}$ and $\beta^{(1)}$ are the angular deviations of the start point of wavevector of the incident X-rays. In reference with Fig. 1, they are described as follows:

$$\overrightarrow{\mathrm{P}_1\mathrm{La}_0} = K\beta^{(0)}\mathbf{e}_0^{(0)} + K\beta^{(1)}\mathbf{e}_0^{(1)}. \tag{9}$$

ξ_i $(= k_i - K)$ is obtained from the scalar product of $\mathbf{s}_i$ and $\mathbf{k}_i - \mathbf{K}_i$. Here, $\mathbf{k}_i = \overrightarrow{\mathrm{P}_1'\mathrm{H}_i}$ and $\mathbf{K}_i = \overrightarrow{\mathrm{La}_0\mathrm{H}_i}$. (5a) can be substituted into the scalar product of $\mathbf{s}_i \cdot \overrightarrow{\mathrm{P}_1'\mathrm{La}_0}$ to obtain the following equation:

$$\xi_i = \mathbf{s}_i \cdot \big(\overrightarrow{\mathrm{P}_1'\mathrm{P}_1} + \overrightarrow{\mathrm{P}_1\mathrm{La}_0}\big) \tag{10a}$$

$$= \xi\mathbf{s}_i \cdot \mathbf{n}_z + K\beta^{(0)}\mathbf{s}_i \cdot \mathbf{e}_0^{(0)} + K\beta^{(1)}\mathbf{s}_i \cdot \mathbf{e}_0^{(1)} \tag{10b}$$

$$= \xi\cos\Theta_i + K\beta^{(0)}S_{i,0}^{(0)} + K\beta^{(1)}S_{i,0}^{(1)}. \tag{10c}$$

(10) can be substituted into the left side of (7) to obtain the following equation:

$$\xi\cos\Theta_i\mathcal{D}_i^{(l)} + K\left(S_{i,0}^{(0)}\beta^{(0)} + S_{i,0}^{(1)}\beta^{(1)}\right)\mathcal{D}_i^{(l)} = \frac{K}{2}\sum_{j=0}^{n-1}\chi_{h_i-h_j}\sum_{m=0}^{1}C_{i,j}^{(l,m)}\mathcal{D}_j^{(m)}. \tag{11}$$

Here, $i, j \in \{0, 1, \cdots, n-1\}$, $n \in \{3, 4, 5, 6, 8, 12\}$ and $l, m \in \{0, 1\}$. Θ_i is the angle spanned by $\mathbf{s}_i$ and $\mathbf{n}_z$. By deviding the both sides of (11) by $\cos\Theta_i$, the following equation can be obtained:

$$\xi\mathcal{D}_i^{(l)} = -\frac{K}{\cos\Theta_i}\left(S_{i,0}^{(0)}\beta^{(0)} + S_{i,0}^{(1)}\beta^{(1)}\right)\mathcal{D}_i^{(l)} + \frac{K}{2\cos\Theta_i}\sum_{j=0}^{n-1}\chi_{h_i-h_j}\sum_{m=0}^{1}C_{i,j}^{(l,m)}\mathcal{D}_j^{(m)}. \tag{12}$$

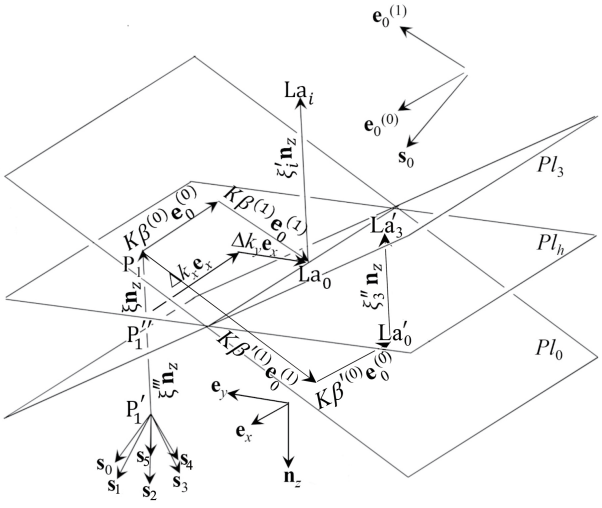

Figure 1: Geometry around the Laue point La_0. Pl_0 and Pl_3 are planes whose distance from H_0 and H_3 is $K(=1/\lambda)$. Pl_h is a plane normal to $\mathbf{n}_z$ (downward surface normal). The Laue point La_0 and the point P_1'' exist on Pl_h. Pl_i $(i \neq \{0,3\})$ were not drawn for simplicity. La_i and La_i' are points whose distance from H_i $(i \in \{0,1,\cdots,n-1\})$ is K. P_1' is the start point of wavevector of the Bloch wave. $\mathrm{P}_{1,k}'$ that appears in equation (51) is the kth numbered P_1' i.e. the start point of wavevector of the kth numbered Bloch wave where $k \in \{1,2,3,\cdots,2n\}$.

(12) can also be described by using matrices and a vector as follows:

$$\xi \mathbf{E} \mathscr{D} = \mathbf{A} \mathscr{D}. \tag{13}$$

Here, $\mathbf{E}$ is a $2n \times 2n$ unit matrix. $\mathscr{D}$ is a $2n$-dimensional column vector whose qth element is $\mathcal{D}_j^{(m)}$ where $q = 2j + m + 1$. Hereafter, eigenvector or matrix whose column vectors are eigenvectors, are symbolized with flower characters. The element of the pth raw and qth column of the $2n \times 2n$ matrix $\mathbf{A}$, $a_{p,q}(p = 2i + l + 1)$ is given as follows:

$$a_{p,q} = \frac{K}{2\cos\Theta_i} \chi_{h_i - h_j} C_{i,j}^{(l,m)} - \frac{\delta_{p,q} K}{\cos\Theta_i} \left(S_{i,0}^{(0)} \beta^{(0)} + S_{i,0}^{(1)} \beta^{(1)} \right). \tag{14}$$

Here, $\delta_{p,q}$ is the Kronecker delta. (13) describes an eigenvalue problem whose $2n$ eigenvalues are ξ and $2n$ eigen vectors are $\mathscr{D}$. ξ restricts the wavevector of the the Bloch wave. $\mathscr{D}$ are amplitude ratios of the Amplitudes. The two-beam E-L theory can also be described as an eigenvalue problem. However, any textbook that describes the two-beam theory as an eigenvalue problem cannot be found. The conventional description of the two-beam dynamical theory has two steps, i.e. description of the dispersion surfaces at first and then (13) is deformed as follows:

$$\left(\mathbf{A} - \xi \mathbf{E} \right) \mathscr{D} = \mathbf{O}. \tag{15}$$

Here, $\mathbf{O}$ are a $2n$-dimensional column vector whose all elements are zero.

$$\det\left(\mathbf{A} - \xi \mathbf{E} \right) = 0. \tag{16}$$

(16) describes the condition for (15) has the solution other than zero vector. In the two-beam case, σ- and π-polarized X-rays can be dealt with independently since they do not interfere with

each other. Further, the term of $j = i$ of the left side of (2) is deleted in general by defining the Lorentz point. The dispersion surfaces described with (16) can be approximated by hyperbolic curves whose cross point of the asymptotes is the Lorentz point. Then, the two-beam E-L theory can be approximately solved analytically. In the description of the present paper, Lorentz point is not defined. There is an advantage that the T-T equation explicitly having the term of $j = i$ can deal with the wave fields in an arbitrary shaped crystal [28]. The dispersion surfaces for the n-beam cases are described by a complex $2n$th order equation whose analytical solution cannot be obtained. This is one of the reason for the late development of the n-beam dynamical theory.

The numerical solution of the n-beam E-L theory has been given by Colella in 1974 [22] for the first time. Colella's method takes into account the curvature of the sphere whose radius is K and center is H_i. This method gives the numerical solution with a higher precision when the start point of the wavevector of Incident X-rays is far distant from the Laue Point in comparison with the method to solve the eigenvalue problem described by (13).

In Fig. 1, La_i whose distance from H_i ($i \in \{6, 7, \cdots, 17\}$) is K, is also described in addition to the Laue point La_0 whose distance from H_0, H_1, H_2, H_3, H_4 and H_5 is K. For later description in §5.7 regarding to the 18-beam case as shown in Fig. 19, the definition of La_i is necessary.

In Fig. 1, $\overrightarrow{\mathrm{La}_0\mathrm{La}_i}$ is parallel to $\overrightarrow{\mathrm{P}'_1\mathrm{P}_1}$. Then, $\xi\mathcal{D}_i^{(l)}$ in the left side of (12) should be replaced with $(\xi + \xi'_i)\mathcal{D}_i^{(l)}$. Here, $\xi'_i = 0$ for $i < 6$. (14) that gives elements of $2n \times 2n$ matrix in (13) should be rewritten as follows:

$$a_{p,q} = \frac{K}{2\cos\Theta_i}\chi_{h_i-h_j}C_{i,j}^{(l,m)} - \frac{\delta_{p,q}K}{\cos\Theta_i}\left(S_{i,0}^{(0)}\beta^{(0)} + S_{i,0}^{(1)}\beta^{(1)}\right) - \delta_{p,q}\xi'_i, \tag{17}$$
$$\text{where, } \xi'_i = 0 \text{ for } i < 6.$$

Fig. 18 (b) has been obtained in the following sequence i.e. i) define the $2n \times 2n$ ($n = 18$) matrix whose elements are as described in (17), ii) solve the eigenvalue problem of (13) and iii) fast Fourier transform the diffraction curves obtained based on (47).

This has an important meaning. In the T-T equation that has been described in 2012 [29], the n reciprocal lattice nodes should be on a circle in the reciprocal space. However, both for the E-L and T-T dynamical theories described in the present paper, the above restriction has been removed.

Further, La'_0 is separately defined in the vicinity of La_0. Then, La'_i ($i \in \{0, 1, 2, \cdots, n-1\}$) are defined on Pl_i such that $\overrightarrow{\mathrm{La}'_0\mathrm{La}'_i} = \xi''_i\mathbf{n}_z$. The n-beam E-L theory corresponding to (11) is described as follows:

$$\xi\cos\Theta_i\mathcal{D}_i'^{(l)} + K\left(S_{i,0}^{(0)}\beta'^{(0)} + S_{i,0}^{(1)}\beta'^{(1)}\right)\mathcal{D}_i'^{(l)}$$
$$= -\xi''_i\cos\Theta_i\mathcal{D}_i'^{(l)} + \frac{K}{2}\sum_{j=0}^{n-1}\chi_{h_i-h_j}\sum_{m=0}^{1}C_{i,j}^{(l,m)}\mathcal{D}_j'^{(m)}, \tag{18}$$
$$\text{where, } i, j \in \{0, 1, \cdots, n-1\},$$
$$n \text{ is number of reciprocal lattice nodes,}$$
$$l, m \in \{0, 1\}.$$

Here, $\overrightarrow{\mathrm{P}_1\mathrm{La}'_0} = K\beta'^{(0)}\mathbf{e}_0^{(0)} + K\beta'^{(1)}\mathbf{e}_0^{(1)}$. The reason for that the first term of the left side of the above equation will be described after deriving (34a) and (34b). The equation corresponding to

(12) is given as follows:

$$\xi \mathcal{D}_i^{\prime(l)} = -\frac{K}{\cos\Theta_i}\left(S_{i,0}^{(0)}\beta^{\prime(0)} + S_{i,0}^{(1)}\beta^{\prime(1)}\right)\mathcal{D}_i^{\prime(l)} - \xi_i^{\prime\prime}\mathcal{D}_i^{\prime(l)} + \frac{K}{2\cos\Theta_i}\sum_{j=0}^{n-1}\chi_{h_i-h_j}\sum_{m=0}^{1}C_{i,j}^{(l,m)}\mathcal{D}_j^{\prime(m)}. \tag{19}$$

Further, (17) can be replaced with the following equation:

$$a_{p,q} = \frac{K}{2\cos\Theta_i}\chi_{h_i-h_j}C_{i,j}^{(l,m)} - \frac{\delta_{p,q}K}{\cos\Theta_i}\left(S_{i,0}^{(0)}\beta^{\prime(0)} + S_{i,0}^{(1)}\beta^{\prime(1)}\right) - \delta_{p,q}\xi_i^{\prime\prime}. \tag{20}$$

(20) can be solved by substituting the above equation into (13) even when n (n is an arbitrary number) reciprocal lattice nodes to be taken into account that exist in the vicinity of the surface of the Ewald sphere.

2.1 Derivation of the the Takagi equation (T-T theory) from the Ewald-Laue (E-L) theory

In this section, the n-beam T-T equation is derived from the n-beam E-L theory described by (11) and/or (12). The exchange of the order of integration in the reciprocal space and differentiation in the real space and that of integration and summation are essential of the discussion.

Let the whole wave field $\tilde{\mathbf{D}}(\mathbf{r})$ i.e. the solution of the dynamical theory be described as follows:

$$\tilde{\mathbf{D}}(\mathbf{r}) = \sum_{i=0}^{n-1}\sum_{l=0}^{1}\mathbf{e}_i^{(l)}D_i^{(l)}(\mathbf{r})\exp\left(-\mathrm{i}2\pi\overrightarrow{\mathrm{La_0H}_i}\cdot\mathbf{r}\right). \tag{21}$$

Here, $\mathbf{r}$ is the location vector. For the later description, let $\mathbf{r}$ be described as a linear combination of $\mathbf{s}_i$, $\mathbf{e}_i^{(0)}$ and $\mathbf{e}_i^{(1)}$ as follows:

$$\mathbf{r} = s_i\mathbf{s}_i + e_i^{(0)}\mathbf{e}_i^{(0)} + e_i^{(1)}\mathbf{e}_i^{(1)}. \tag{22}$$

The amplitude of the ith numbered wave with polarization state of l can be described as follows:

$$\mathcal{D}_i^{(l)}(\Delta\mathbf{k})\exp\left(-\mathrm{i}2\pi\overrightarrow{\mathrm{P}_1^{\prime}\mathrm{H}_i}\cdot\mathbf{r}\right) = \mathcal{D}_i^{(l)}(\Delta\mathbf{k})\exp\left(-\mathrm{i}2\pi\Delta\mathbf{k}\cdot\mathbf{r}\right)\exp\left(-\mathrm{i}2\pi\overrightarrow{\mathrm{La_0H}_i}\cdot\mathbf{r}\right), \tag{23}$$

where $\Delta\mathbf{k} = \overrightarrow{\mathrm{P}_1^{\prime}\mathrm{La}_0}$.

Let us decribe the amplitudes of Bloch waves $\mathcal{D}_i^{(l)}$ as $\mathcal{D}_i^{(l)}(\Delta\mathbf{k})$ to clartify these amplitudes are functions of $\Delta\mathbf{k}$. Further, for later description, let us confirm that $\Delta\mathbf{k}$ are described from (8) and (9) as follows:

$$\Delta\mathbf{k} = \xi\mathbf{n}_z + K\beta^{(0)}\mathbf{e}_0^{(0)} + K\beta^{(1)}\mathbf{e}_0^{(1)}. \tag{24}$$

$\mathcal{D}_i^{(l)}(\Delta\mathbf{k})$ can be an arbitrary function of $\Delta\mathbf{k}$. For example, $\mathcal{D}_i^{(l)}(\Delta\mathbf{k})$ is the Dirac delta function of $\Delta\mathbf{k}$ for the condition of plane wave incidence. However, the constant function whose amplitude and phase do not change depending on $\Delta\mathbf{k}$ for the condition of spherical wave incidence.

Since $D_i^{(l)}(\mathbf{r})$ and $D_j^{(m)}(\mathbf{r})$ are the amplitudes of the ith and jth numbered waves whose polarization states are l and m are considered to be coherent superpositions of Bloch waves, they are described as follows:

$$D_i^{(l)}(\mathbf{r}) = \int_{\Delta\mathbf{k}}^{D.S.} \mathcal{D}_i^{(l)}(\Delta\mathbf{k}) \exp\left(-\mathrm{i}2\pi\Delta\mathbf{k}\cdot\mathbf{r}\right) \mathrm{d}S, \tag{25a}$$

$$D_j^{(m)}(\mathbf{r}) = \int_{\Delta\mathbf{k}}^{D.S.} \mathcal{D}_j^{(m)}(\Delta\mathbf{k}) \exp\left(-\mathrm{i}2\pi\Delta\mathbf{k}\cdot\mathbf{r}\right) \mathrm{d}S. \tag{25b}$$

Here, $\int_{\Delta k}^{D.S.} \mathrm{d}S$ means the integration over the dispersion surfaces. Since there are $2n$ couples of dispersion surfaces and eigenvectors, they can be described as $\sum_{k=1}^{2n}\int_{\Delta k}^{D.S.} \mathrm{d}S$. However, (25) has been described under the assumption that $\int_{\Delta k}^{D.S.} \mathrm{d}S$ means an integration for $2n$ dispersion surfaces in (25a) and (25b) for simplicity in the later deformation of the equations. $D_i^{(l)}(\mathbf{r})$ and $D_j^{(m)}(\mathbf{r})$ are the amplitudes that modulate the waves of $\exp(-\mathrm{i}2\pi\overrightarrow{\mathrm{La_0H}_i}\cdot\mathbf{r})\ \mathbf{e}_i^{(l)}$ and $\exp(-\mathrm{i}2\pi\overrightarrow{\mathrm{La_0H}_j}\cdot\mathbf{r})\ \mathbf{e}_j^{(m)}$, respectively. By substituting (22) and (24) and considering the polarization factors defined as in (5a), the following equation can be obtained:

$$\begin{aligned} D_i^{(l)}(\mathbf{r}) = &\int_{\Delta\mathbf{k}}^{D.S.} \mathcal{D}_i^{(l)}(\Delta\mathbf{k}) \\ &\times \exp\Big\{ -\mathrm{i}2\pi\Big[\Big(\xi\cos\Theta_i + K\beta^{(0)}S_{i,0}^{(0)} + K\beta^{(1)}S_{i,0}^{(1)}\Big)s_i + f_i\big(e_i^{(0)}, e_i^{(1)}\big)\Big]\Big\}\mathrm{d}S. \end{aligned} \tag{26}$$

Here, $f_i\big(e_i^{(0)}, e_i^{(1)}\big)$ are functions of $e_i^{(0)}$, $e_i^{(1)}$ that do not depend on s_i. Therefore, $\partial D_i^{(l)}(\mathbf{r})/\partial s_i$ can be calculated as follows:

$$\frac{\partial}{\partial s_i} D_i^{(l)}(\mathbf{r}) = \frac{\partial}{\partial s_i} \int_{\Delta\mathbf{k}}^{D.S.} \mathcal{D}_i^{(l)}(\Delta\mathbf{k}) \exp\left(-\mathrm{i}2\pi\Delta\mathbf{k}\cdot\mathbf{r}\right) \mathrm{d}S \tag{27a}$$

$$= \int_{\Delta\mathbf{k}}^{D.S.} \frac{\partial}{\partial s_i} \Big[\mathcal{D}_i^{(l)}(\Delta\mathbf{k}) \exp\left(-\mathrm{i}2\pi\Delta\mathbf{k}\cdot\mathbf{r}\right)\Big] \mathrm{d}S \tag{27b}$$

$$\begin{aligned} = -\mathrm{i}2\pi \int_{\Delta\mathbf{k}}^{D.S.} &\Big[\xi\cos\Theta_i + K\Big(S_{i,0}^{(0)}\beta^{(0)} + S_{i,0}^{(1)}\beta^{(1)}\Big)\Big] \\ &\times \mathcal{D}_i^{(l)}(\Delta\mathbf{k}) \exp\left(-\mathrm{i}2\pi\Delta\mathbf{k}\cdot\mathbf{r}\right) \mathrm{d}S. \end{aligned} \tag{27c}$$

On the other hand, in place of $\Delta\mathbf{k}$ in (24), let define $\Delta\mathbf{k}'$ as follows:

$$\Delta\mathbf{k}' = \overrightarrow{\mathrm{P_1'La_0'}} \tag{28a}$$

$$= \xi\mathbf{n}_z + K\beta'^{(0)}\mathbf{e}_0^{(0)} + K\beta'^{(1)}\mathbf{e}_0^{(1)}. \tag{28b}$$

In (25) and (26), $\Delta\mathbf{k}$, $\mathcal{D}_i^{(l)}(\Delta\mathbf{k})$, $D_j^{(m)}(\mathbf{r})$, $\mathcal{D}_j^{(m)}(\Delta\mathbf{k})$, $\beta^{(0)}$ and $\beta^{(1)}$ can be replaced with $\Delta\mathbf{k}'$, $D_i'^{(l)}(\mathbf{r})$, $\mathcal{D}_i'^{(l)}(\Delta\mathbf{k}')$, $D_j'^{(m)}(\mathbf{r})$, $\mathcal{D}_j'^{(m)}(\Delta\mathbf{k}')$, $\beta'^{(0)}$ and $\beta'^{(1)}$ to obtain the following equation:

$$\begin{aligned} \frac{\partial}{\partial s_i} D_i'^{(l)}(\mathbf{r}) = -\mathrm{i}2\pi \int_{\Delta\mathbf{k}'}^{D.S.} &\Big[\xi\cos\Theta_i + K\Big(S_{i,0}^{(0)}\beta'^{(0)} + S_{i,0}^{(1)}\beta'^{(1)}\Big)\Big] \\ &\times \mathcal{D}_i'^{(l)}(\Delta\mathbf{k}') \exp\left(-\mathrm{i}2\pi\Delta\mathbf{k}'\cdot\mathbf{r}\right) \mathrm{d}S. \end{aligned} \tag{29}$$

When n reciprocal lattice nodes exist on a circle in the reciprocal space, $D_i^{(l)}(\mathbf{r})$ in (27) is the amplitude that modulates the oscillation of $\exp\big(-\mathrm{i}2\pi\ \overrightarrow{\mathrm{La_0H}_i}\cdot\mathbf{r}\big)\ \mathbf{e}_i^{(l)}$. However, $D_i'^{(l)}(\mathbf{r})$ in (29)

is the amplitude that modulates the oscillation of $\exp\big(-\mathrm{i}2\pi\ \overrightarrow{\mathrm{La}_0'\mathrm{H}_i}\cdot\mathbf{r}\big)\ \mathbf{e}_i^{(l)}$. (29) has been derived to generalize the T-T equation in the later description such as to take into account all reciprocal lattice nodes in the vicinity of the surface of the Ewald sphere.

By substituting (11) into (27), the following equations can be obtained:

$$\frac{\partial}{\partial s_i}D_i^{(l)}(\mathbf{r}) = -\mathrm{i}\pi K\int_{\Delta\mathbf{k}}^{D.S.}\sum_{j=0}^{n-1}\chi_{h_i-h_j}\sum_{m=0}^{1}C_{i,j}^{(l,m)}\mathcal{D}_j^{(m)}(\Delta\mathbf{k})\exp\left(-\mathrm{i}2\pi\Delta\mathbf{k}\cdot\mathbf{r}\right)\mathrm{d}S \tag{30a}$$

$$= -\mathrm{i}\pi K\sum_{j=0}^{n-1}\chi_{h_i-h_j}\sum_{m=0}^{1}C_{i,j}^{(l,m)}\int_{\Delta\mathbf{k}}^{D.S.}\mathcal{D}_j^{(m)}(\Delta\mathbf{k})\exp\left(-\mathrm{i}2\pi\Delta\mathbf{k}\cdot\mathbf{r}\right)\mathrm{d}S. \tag{30b}$$

(25b) can be substituted into (30) to obtain the following equation:

$$\frac{\partial}{\partial s_i}D_i^{(l)}(\mathbf{r}) = -\mathrm{i}\pi K\sum_{j=0}^{n-1}\chi_{h_i-h_j}\sum_{m=0}^{1}C_{i,j}^{(l,m)}D_j^{(m)}(\mathbf{r}), \tag{31}$$

$$\text{where,}\quad i,j\in\{0,1,\cdots,n-1\},$$
$$n\in\{3,4,5,6,8,12\},$$
$$l,m\in\{0,1\}.$$

The above equation (31) is the n-beam T-T equation applicable to the cases where n reciprocal lattice nodes exist on an identical circle in the reciprocal space.

Incidentally, in the case of a perfect crystal, the electric susceptibility in the crystal $\chi(\mathbf{r})$ can be Fourier-expanded to be $\chi(\mathbf{r})=\sum_i\chi_{h_i}\exp\big(-\mathrm{i}2\pi\mathbf{h}_i\cdot\mathbf{r}\big)$. However, in the cases that the crystal has the lattice displacement field $\mathbf{u}(\mathbf{r})$, the electric susceptibility is approximately Fourier-expanded as follows:

$$\chi\big[\mathbf{r}-\mathbf{u}(\mathbf{r})\big] = \sum_i\chi_{h_i}\exp\big\{-\mathrm{i}2\pi\mathbf{h}_i\cdot\big[\mathbf{r}-\mathbf{u}(\mathbf{r})\big]\big\} \tag{32a}$$

$$= \sum_i\chi_{h_i}\exp\big[\mathrm{i}2\pi\mathbf{h}_i\cdot\mathbf{u}(\mathbf{r})\big]\exp\big(-\mathrm{i}2\pi\mathbf{h}_i\cdot\mathbf{r}\big). \tag{32b}$$

Then, when the crystal has the lattice displacement field of $\mathbf{u}(\mathbf{r})$, the Fourier coefficient of the electric susceptibility is a function of the position in the crystal, can be described as $\chi_{h_i-h_j}\exp\big[\mathrm{i}\,2\pi(\mathbf{h}_i-\mathbf{h}_j)\cdot\mathbf{u}(\mathbf{r})\big]$. Therefore, (31) can be deformed for a crystal having the lattice displacement field as follows:

$$\frac{\partial}{\partial s_i}D_i^{(l)}(\mathbf{r}) = -\mathrm{i}\pi K\sum_{j=0}^{n-1}\chi_{h_i-h_j}\exp\big[\mathrm{i}2\pi(\mathbf{h}_i-\mathbf{h}_j)\cdot\mathbf{u}(\mathbf{r})\big]\sum_{m=0}^{1}C_{i,j}^{(l,m)}D_j^{(m)}(\mathbf{r}). \tag{33}$$

The above equation (33) is nothing but the n-beam T-T equation [27,29] that can deal with the X-ray wave fields in a deformed crystal in the case that n reciprocal lattice nodes exist on an identical circle in the reciprocal space [27,29].

Next, let us derive the n-beam T-T equation to take into account the all reciprocal lattice nodes in the vicinity of the surface of the Ewald sphere.

As decribed just before deriving (18), La_0' is the 0th-numbered 'generalized Laue point' that exist on Pl_0 in Fig. 1. As described before, $\overrightarrow{\mathrm{La}_0'\mathrm{La}_i'}$ is $\xi_i''\mathbf{n}_z$ (see Fig. 1). For the case that n reciprocal lattice nodes exist on an identical circle in the reciprocal space, (11) has been

substituted into (27) to obtain (30). To generalize the n-beam T-T equation such as to take into account the all reciprocal lattice nodes in the vicinity of the surface of the Ewald sphere, (18) can be substituted into (29) to obtain the following equation:

$$\frac{\partial}{\partial s_i}D_i^{\prime(l)}(\mathbf{r}) = \mathrm{i}2\pi\xi_i^{\prime\prime}\cos\Theta_i\int_{\Delta\mathbf{k}'}^{D.S.}\mathcal{D}_i^{\prime(l)}(\Delta\mathbf{k}')\exp\big[-\mathrm{i}2\pi\Delta\mathbf{k}'\cdot\mathbf{r}\big]\mathrm{d}S$$
$$-\mathrm{i}\pi K\int_{\Delta\mathbf{k}'}^{D.S.}\sum_{j=0}^{n-1}\chi_{h_i-h_j}\sum_{m=0}^{1}C_{i,j}^{(l,m)}\mathcal{D}_j^{\prime(m)}(\Delta\mathbf{k}')\exp\big(-\mathrm{i}2\pi\Delta\mathbf{k}'\cdot\mathbf{r}\big)\,\mathrm{d}S \tag{34a}$$
$$=\mathrm{i}2\pi\xi_i^{\prime\prime}\cos\Theta_i D_i^{\prime(l)}(\mathbf{r})-\mathrm{i}\pi K\sum_{j=0}^{n-1}\chi_{h_i-h_j}\sum_{m=0}^{1}C_{i,j}^{(l,m)}D_j^{\prime(m)}(\mathbf{r}), \tag{34b}$$

where, $i,j\in\{0,1,\cdots,n-1\}$,
n is the number of reciproca lattice nodes,
$l,m\in\{0,1\}$.

At first glance, it might seem like the calculation can be simplified by putting that $\Delta\mathbf{k}_i'=\overrightarrow{\mathrm{P}_1'\mathrm{La}_i'}$ to change the contents of the integration of the right side of (25a) to be $\mathcal{D}_i^{\prime(l)}(\Delta\mathbf{k}_i')\exp(-\mathrm{i}2\pi\Delta\mathbf{k}_i'\cdot\mathbf{r})$. However, in this case, the second term of (34a) cannot be deformed to be the second term of (34b) since the contents of the integration in the right side of (25b) should be $\mathcal{D}_j^{(m)}(\Delta\mathbf{k}_j')\exp(-\mathrm{i}2\pi\Delta\mathbf{k}_j'\cdot\mathbf{r})$ to keep the symmetry of the equation. For this reason, the first term of the right side of (18) has not been transferred to the left side. Then, based on (32), the following equation is obtained:

$$\frac{\partial}{\partial s_i}D_i^{\prime(l)}(\mathbf{r}) = \mathrm{i}2\pi\xi_i^{\prime\prime}\cos\Theta_i D_i^{\prime(l)}(\mathbf{r})$$
$$-\mathrm{i}\pi K\sum_{j=0}^{n-1}\chi_{h_i-h_j}\exp\big[\mathrm{i}2\pi(\mathbf{h}_i-\mathbf{h}_j)\cdot\mathbf{u}(\mathbf{r})\big]\sum_{m=0}^{1}C_{i,j}^{(l,m)}D_j^{\prime(m)}(\mathbf{r}). \tag{35}$$

The above equation (35) is the n-beam T-T equation that describes the X-ray wave fields in a crystal that has lattice displacement field by taking into account all reciprocal lattice nodes in the vicinity of the surface of the Ewald sphere.

Now let us derive the equation applicable for the case that plane wave X-rays are incident on the crystal. $D_i^{\prime(l)}(\mathbf{r})$ and $D_j^{\prime(m)}(\mathbf{r})$ in (34b) are X-ray amplitudes that modulate the oscillations of $\exp(-\mathrm{i}2\pi\ \overrightarrow{\mathrm{La}_0'\mathrm{H}_i}\cdot\mathbf{r})\ \mathbf{e}_i^{(l)}$ and $\exp(-\mathrm{i}2\pi\ \overrightarrow{\mathrm{La}_0'\mathrm{H}_j}\cdot\mathbf{r})\ \mathbf{e}_j^{(m)}$, respectively. $D_i^{\prime\prime(l)}(\mathbf{r})$ and $D_j^{\prime\prime(m)}(\mathbf{r})$ are X-ray amplitudes that modulate the oscillations of $\exp(-\mathrm{i}2\pi\ \overrightarrow{\mathrm{P}_1\mathrm{H}_i}\cdot\mathbf{r})\ \mathbf{e}_i^{(l)}$ and $\exp(-\mathrm{i}2\pi\ \overrightarrow{\mathrm{P}_1\mathrm{H}_j}\cdot\mathbf{r})\ \mathbf{e}_j^{(m)}$. In reference to Fig. 1, we can understand the following relations

$$D_i^{\prime(l)}(\mathbf{r}) = D_i^{\prime\prime(l)}(\mathbf{r})\exp\big(-\mathrm{i}2\pi\overrightarrow{\mathrm{P}_1\mathrm{La}_0'}\cdot\mathbf{r}\big) \tag{36a}$$
$$= D_i^{\prime\prime(l)}(\mathbf{r})\exp\big[-\mathrm{i}2\pi K\big(\beta^{\prime(0)}\mathbf{e}_0^{(0)}+\beta^{\prime(1)}\mathbf{e}_0^{(1)}\big)\cdot\mathbf{r}\big], \tag{36b}$$
$$D_j^{\prime(m)}(\mathbf{r}) = D_j^{\prime\prime(m)}(\mathbf{r})\exp\big(-\mathrm{i}2\pi\overrightarrow{\mathrm{P}_1\mathrm{La}_0'}\cdot\mathbf{r}\big). \tag{36c}$$

The both sides of (36b) can be partially differentiated as follows:

$$\frac{\partial}{\partial s_i}D_i^{\prime(l)}(\mathbf{r}) = \Big[\frac{\partial}{\partial s_i}D_i^{\prime\prime(l)}(\mathbf{r})\Big]\exp\big(-\mathrm{i}2\pi\overrightarrow{\mathrm{P}_1\mathrm{La}_0'}\cdot\mathbf{r}\big)$$
$$-\mathrm{i}2\pi K\big(\beta^{\prime(0)}S_{i,0}^{(0)}+\beta^{\prime(1)}S_{i,0}^{(1)}\big)D_i^{\prime\prime(l)}(\mathbf{r})\exp\big(-\mathrm{i}2\pi\overrightarrow{\mathrm{P}_1\mathrm{La}_0'}\cdot\mathbf{r}\big). \tag{37}$$

(36a), (36b) and (37) can be substituted into (34b) to obtain the following equation:

$$\frac{\partial}{\partial s_i} D_i''^{(l)}(\mathbf{r}) = \mathrm{i}2\pi\xi_i'' \cos\Theta_i D_i''^{(l)}(\mathbf{r}) + \mathrm{i}2\pi K\left(\beta'^{(0)} S_{i,0}^{(0)} + \beta'^{(1)} S_{i,0}^{(1)}\right) D_i''^{(l)}(\mathbf{r}) - \mathrm{i}\pi K \sum_{j=0}^{n-1} \chi_{h_i-h_j} \sum_{m=0}^{1} C_{i,j}^{(l,m)} D_j''^{(m)}(\mathbf{r}). \tag{38}$$

$D_i''^{(l)}(\mathbf{r})$ and $D_j''^{(m)}(\mathbf{r})$ in the above equation (38) are X-ray amplitudes that modulate the oscillations of $\exp\left(-\mathrm{i}2\pi\ \overrightarrow{\mathrm{P_1H}_i}\cdot\mathbf{r}\right)\mathbf{e}_i^{(l)}$ and $\exp\left(-\mathrm{i}2\pi\ \overrightarrow{\mathrm{P_1H}_j}\cdot\mathbf{r}\right)\mathbf{e}_j^{(m)}$. Under the condition that plane wave X-rays whose wavevector is $\overrightarrow{\mathrm{P_1H}_0}$ are incident on the crystal, a constant value of $D_0''^{(0)}(\mathbf{r})$ and/or $D_0''^{(1)}(\mathbf{r})$ should be given as the boundary condition depending on the polarization state of the incident X-rays.

When the downward surface normal of the crystal is $\mathbf{n}_z$ and unit vectors $\mathbf{e}_x$ and $\mathbf{e}_y$ are defined such that $\mathbf{e}_x$, $\mathbf{e}_y$ and $\mathbf{n}_z$ construct a right-handed orthogonal system in this order and the location vector $\mathbf{r}= x\mathbf{e}_x + y\mathbf{e}_y + z\mathbf{n}_z$, the X-ray amplitudes obtained by solving (38) are the function of only z not depending on the values of x and y. Therefore, they can be described as $D_i''^{(l)}(z)$ and $D_j''^{(m)}(z)$. Then, $\partial D_i''^{(l)}(\mathbf{r})/\partial s_i$ in the left side of (38) can be deformed as follows:

$$\frac{\partial D_i''^{(l)}(\mathbf{r})}{\partial s_i} = \mathbf{s}_i \cdot \left(\frac{\mathrm{d}D_i''^{(l)}(z)}{\mathrm{d}z}\right)\mathbf{n}_z \tag{39a}$$

$$= \cos\Theta_i \frac{\mathrm{d}D_i''^{(l)}(z)}{\mathrm{d}z}. \tag{39b}$$

(39) can be substituted into (38) to obtain the ordinary differential equation as follows:

$$\frac{\mathrm{d}}{\mathrm{d}z} D_i''^{(l)}(z) = \mathrm{i}2\pi\xi_i'' D_i''^{(l)}(z) + \frac{\mathrm{i}2\pi K}{\cos\Theta_i}\left(\beta'^{(0)} S_{i,0}^{(0)} + \beta'^{(1)} S_{i,0}^{(1)}\right) D_i''^{(l)}(z) - \frac{\mathrm{i}\pi K}{\cos\Theta_i} \sum_{j=0}^{n-1} \chi_{h_i-h_j} \sum_{m=0}^{1} C_{i,j}^{(l,m)} D_j''^{(m)}(z). \tag{40}$$

(40) can be described also as an eigenvalue problem whose numerical solution can be obtained by using the numerical subroutine libralies e.g. LAPACK. Also from this, the equivalence between the E-L and T-T theories can be verified. However, the details of this are not described here.

2.2 Derivation of the Ewald-Laue (E-L) theory from the Takagi-Taupin (T-T) equation

In this section, the n-beam E-L theory described in (11) and/or (12) is derived from the n-beam T-T equation described in (31).

When plane wave X-rays are incident on the crystal to excite $2n$ tie points on the dispersion surfaces, total wave field $\tilde{\boldsymbol{\mathcal{D}}}$ is described as the summation of Bloch waves as follows:

$$\tilde{\boldsymbol{\mathcal{D}}} = \sum_{i=0}^{n-1} \sum_{l=0}^{1} \mathbf{e}_i^{(l)} \mathcal{D}_i^{(l)}(\Delta\mathbf{k}) \exp\left(-\mathrm{i}2\pi\Delta\mathbf{k}\cdot\mathbf{r}\right) \exp\left(-\mathrm{i}2\pi\overrightarrow{\mathrm{La_0H}_i}\cdot\mathbf{r}\right). \tag{41}$$

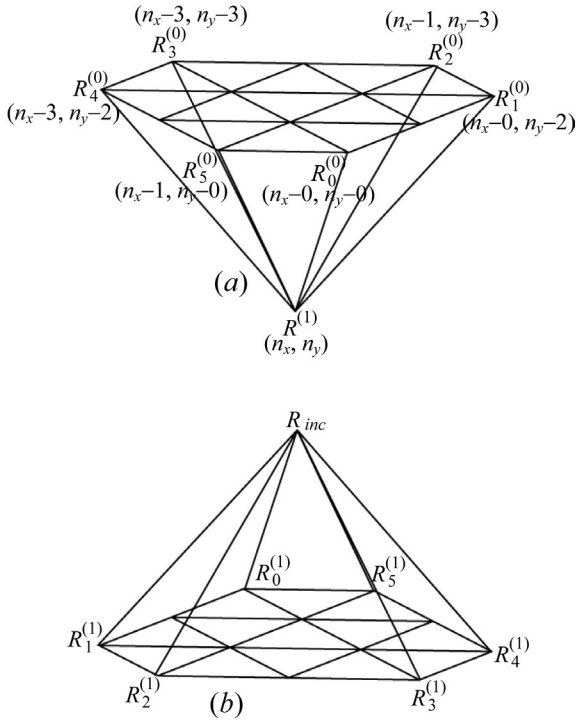

Figure 2: These figures show small hexagonal pyramids used when solving the n-beam T-T equation (31) in a six-beam case whose results are shown in Fig. 12 [reproduction of Fig. 1 in Okitsu, Imai and Yoda (2012)].

Here, $D_i^{(l)}(\mathbf{r}) = \mathcal{D}_i^{(l)}(\Delta\mathbf{k})\exp(-\mathrm{i}2\pi\overrightarrow{\mathrm{P_1H}_i}\cdot\mathbf{r})$ and $D_j^{(m)}(\mathbf{r}) = \mathcal{D}_j^{(m)}(\Delta\mathbf{k})\exp(-\mathrm{i}2\pi\overrightarrow{\mathrm{P_1H}_j}\cdot\mathbf{r})$. Therefore,

$$\frac{\partial}{\partial s_i}\left[\mathcal{D}_i^{(l)}(\Delta\mathbf{k})\exp\left(-\mathrm{i}2\pi\Delta\mathbf{k}\cdot\mathbf{r}\right)\right] = -\mathrm{i}\pi K\sum_{j=0}^{n-1}\chi_{h_i-h_j}\sum_{m=0}^{1}C_{i,j}^{(l,m)}\left[\mathcal{D}_j^{(m)}(\Delta\mathbf{k})\exp\left(-\mathrm{i}2\pi\Delta\mathbf{k}\cdot\mathbf{r}\right)\right]. \tag{42}$$

However, the left side of (42) can be deformed in the same procedure used when deriving (26) as follows:

$$\frac{\partial}{\partial s_i}\left[\mathcal{D}_i^{(l)}(\Delta\mathbf{k})\exp\big(-\mathrm{i}2\pi\Delta\mathbf{k}\cdot\mathbf{r}\big)\right] = \mathcal{D}_i^{(l)}(\Delta\mathbf{k})\frac{\partial}{\partial s_i}\exp\Big\{-\mathrm{i}2\pi\Big[\big(\xi\cos\Theta_i + K\beta^{(0)}S_{i,0}^{(0)} + K\beta^{(1)}S_{i,0}^{(1)}\big)s_i + f_i\big(e_i^{(0)},e_i^{(1)}\big)\Big]\Big\} \tag{43a}$$

$$= -\mathrm{i}2\pi\Big(\xi\cos\Theta_i + K\beta^{(0)}S_{i,0}^{(0)} + K\beta^{(1)}S_{i,0}^{(1)}\Big)\mathcal{D}_i^{(l)}(\Delta\mathbf{k})\exp\big(-\mathrm{i}2\pi\Delta\mathbf{k}\cdot\mathbf{r}\big). \tag{43b}$$

The right hands of (42) and (43) can be compared to obtain the same equation as (11). The equivalence between the E-L and T-T theories that can be described by the Fourier transform, has been verified explicitly from the descriptions of the previous and present subsections.

As far as the present author knows, just a short statement concerning this relation between the E-L and T-T theories for the two-beam case can be found only in §11.3 of Authier's book [8].

3 Numerical method to solve the n-beam dynamical theories

3.1 Numerical method to solve the n-beam T-T equation

In reference to Fig. 2 (a) and 2 (b), the algorithm to solve the n-beam T-T equation as described in (31) for $n = 6$ is explained. The following method was used to obtain the computer-simulated images shown in Fig. 12. $\overrightarrow{R_i^{(0)}R^{(1)}}$ in Fig. 2 (a) is parallel to $\mathbf{s}_i$. When the length of $\overrightarrow{R_i^{(0)}R^{(1)}}$ is sufficiently small compared with the value of $|-1/(\chi_0 K)|$, the n-beam T-T equation can be approximated by the following equation:

$$\frac{D_i^{(l)}(R^{(1)}) - D_i^{(l)}(R_i^{(0)})}{\left|\overrightarrow{R_i^{(0)}R^{(1)}}\right|} = -\mathrm{i}\pi K\sum_{j=0}^{n-1}\chi_{h_i-h_j}\sum_{m=0}^{1}C_{i,j}^{(l,m)}\frac{D_j^{(m)}(R_i^{(0)}) + D_j^{(m)}(R^{(1)})}{2}. \tag{44}$$

(44) describes $2n$-dimensional simultaneous linear equations for ($i \in \{0,1,\cdots,n-1\}$, $l \in \{0,1\}$) and can be numerically solved by using subroutine e.g. ZGeTRF and ZGeTRS in the lapack (Linear Algebra subroutine library Package).

Fig. 3 is the top view of Fig. 2 (b). In this case, 0 0 0-forward diffracted, $\overline{4}$ 0 4, $\overline{4}$ 2 6, 0 6 6, 2 6 4 and 2 2 0-reflected X-ray beams are simultaneously strong (see Fig. 12). The angle spanned by the directions of n_x and n_y is 120°. Vectors $\overrightarrow{R_{inc}R_i^{(1)}}$ ($i \in \{0,1,2,3,4,5\}$) in Fig. 2 (b) are parallel to the directions of propagations of 0 0 0-forward diffracted, $\overline{4}$ 0 4, $\overline{4}$ 2 6, 0 6 6, 2 6 4 and 2 2 0-reflected X-ray beams. A four-dimensional array $D_{even}(i,l,n_x,n_y)$ [$i \in \{0,1,\cdots,n-1\}$, $l \in \{0,1\}$, $n_x \in \{\cdots,-2,-1,0,1,2,\cdots\}$, $n_y \in \{\cdots,-2,-1,0,1,2,\cdots\}$] should be prepared such that the calculated X-ray amplitudes are saved. Here, i is the ordinal number of the X-ray

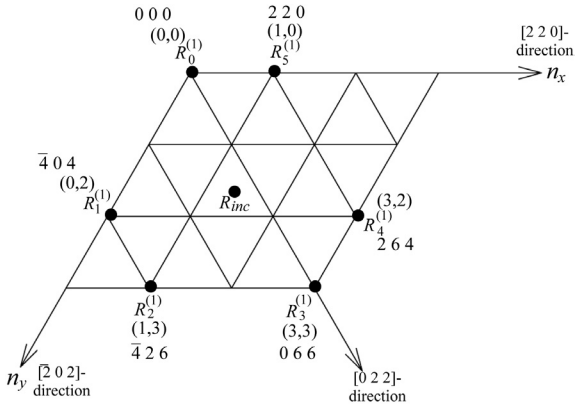

Figure 3: This figure shows a top view of Fig. 2 (b) (reproduction of Fig. 2 in Okitsu *et al.* (2012) [29]).

wave, l ($l \in \{0, 1\}$) is the polarization state, n_x and n_y are two-dimensional positions on the layer in the crystal. The crystal is divided to sufficiently large number of layers. The calculations are repeated layer by layer toward the depth direction. As shown in Fig. 2 (a), X-ray amplitudes $D_{odd}(j, m, n_x, n_y)$ just below the crystal surface can be obtained from $D_{odd}(i, l, n_x - 0, n_y - 0)$, $D_{odd}(i, l, n_x - 0, n_y - 2)$, $D_{odd}(i, l, n_x - 1, n_y - 3)$, $D_{odd}(i, l, n_x - 3, n_y - 3)$, $D_{odd}(i, l, n_x - 3, n_y - 2)$, and $D_{odd}(i, l, n_x - 1, n_y - 0)$ by solving (44). Outside the Borrmann pyramid as shown in Fig. 2 (b), the wave fields do not exist. The calculation is performed by scanning insid the Bormann pyramid. The values of $\chi_{h_i - h_j}$ were calculated by using XOP version 2.3 [34]

The difference equation that approximates the standard differential equation (40) is given as follows:

$$\frac{D_i''^{(l)}(z + \Delta z) - D_i''^{(l)}(z)}{\Delta z} = \mathrm{i}2\pi \left[\xi_i'' + \frac{K}{\cos\Theta_i} \left(\beta'^{(0)} S_{i,0}^{(0)} + \beta'^{(1)} S_{i,0}^{(1)} \right) \right] \frac{D_i''^{(l)}(z) + D_i''^{(l)}(z + \Delta z)}{2} - \frac{\mathrm{i}\pi K}{\cos\Theta_i} \sum_{j=0}^{n-1} \chi_{h_i - h_j} \sum_{m=0}^{1} C_{i,j}^{(l,m)} \frac{D_j''^{(m)}(z) + D_j''^{(m)}(z + \Delta z)}{2}. \tag{45}$$

(45) can be solved in a short time only when incident plane-wave X-rays excite n diffracted X-ray beams all in Laue geometries.

3.2 Numerical method to solve the n-beam E-L theory

After substituting (14) into matrix $\mathbf{A}$ of (13), kth ($k \in \{1, 2, \cdots, 2n\}$) eigenvalue ξ_k and eigenvector $\boldsymbol{\mathscr{D}}_k$ can be solved by using subroutine libraries e.g. LAPACK.

In this way, wave vectors and amplitude ratios of the qth $\left(q = 2j + m + 1\right)$ Bloch wave. On the other hand, mixing ratio of $2n$ Bloch waves should be calculated such as to satisfy the boundary condition.

After making $2n \times 2n$ matrix $\boldsymbol{\mathscr{D}}$ whose element of qth raw and kth column is $\mathscr{D}_{q,k}$ $(= \mathscr{D}_{j,k}^{(m)})$, the following equation is obtained:

$$\boldsymbol{\mathscr{D}} \boldsymbol{\alpha}^{(0)} = \left(1, 0, 0, \cdots, 0, 0\right)^T, \tag{46a}$$

$$\boldsymbol{\mathscr{D}} \boldsymbol{\alpha}^{(1)} = \left(0, 1, 0, \cdots, 0, 0\right)^T. \tag{46b}$$

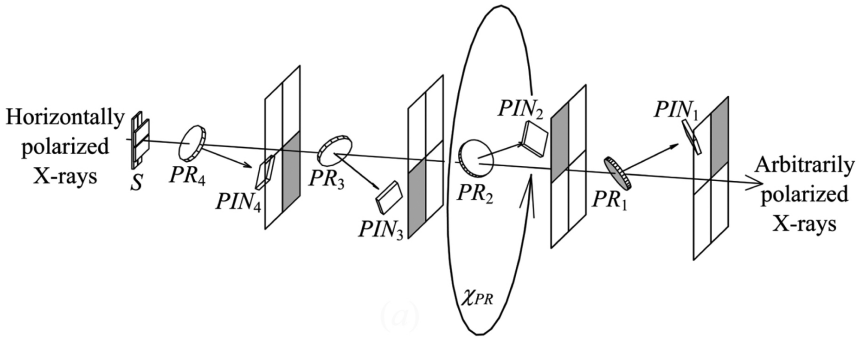

Figure 4: Schematic drawing of the 'rotating four-quadrant phase retarder system' (reproduction of Fig. 3 in Okitsu *et al.* (2006) [27]).

The above equations (46a) and (46b) are the boundary conditions that should be given for the entrance surface when an X-ray beam whose polarization state is l ($l \in \{0, 1\}$) is incident on the crystal. These equations can be solved to obtain the kth element $\alpha_k^{(l)}$ of the column vector $\boldsymbol{\alpha}^{(l)}$. These are mixing ratios of kth Bloch waves. Then, the amplitudes $\mathcal{D}_j^{(l,m)}(exit)$ $\left[= \mathcal{D}_q^{(l)}(exit)\right]$ of the jth numbered X-ray beam whose polarization state is m, can be obtained as follows:

$$\mathcal{D}_j^{(l,m)}(exit) = \mathcal{D}_q^{(l)}(exit) \tag{47a}$$

$$= \sum_{k=1}^{2n} \alpha_k^{(l)} \mathscr{D}_{j,k}^{(m)} \exp[-\mathrm{i}2\pi\xi_k T_z]. \tag{47b}$$

Here, T_z is the thickness of the crystal.

The second terms $\beta^{(0)}$ and $\beta^{(1)}$ in the left side of (14) are angular deviations from the exact n-beam condition. Two-dimensional rocking curves are obtained as shown in Fig. Fig. 10 by calculating $\left|\mathcal{D}_j^{(l,m)}(exit)\right|^2 \left(\mathbf{n}_z \cdot \mathbf{s}_j\right) / \left(\mathbf{n}_z \cdot \mathbf{s}_0\right)$ as the intensities of the jth numbered X-ray beam. $\left(\mathbf{n}_z \cdot \mathbf{s}_j\right) / \left(\mathbf{n}_z \cdot \mathbf{s}_0\right)$ is the correction term for taking into account the difference in the area of the cross section for the X-ray beams. $j = 0$ in the case of Fig. 10.

When the jth numbered X-rays are reflected in the Bragg geometry, the boundary condition should be given to be $\sum_{k=1}^{2n} \alpha_k^{(l)} \mathscr{D}_{j,k}^{(m)} \exp\left(-\mathrm{i}2\pi\xi_k T_z\right) = 0$ such that the summation of the amplitudes is zero.

In the present author's and his coauthors papers published in 2019 [35, 36] report pinhole topograph images obtained by fast Fourier-transforming the solution of the E-L theory. This method was developed by Kohn & Khikhlukha [37] and by Kohn [38]. They reported computer-simulated pinhole topographs for a symmetric six-beam case. The present author and his coauthors extended this method such as to deal with a 18-beam case in which 18 reciprocal lattice nodes do not exist on an identical circle in the reciprocal space. Here, let the location vector on the exit surface $\mathbf{r}_{exit}$ be described as follows:

$$\mathbf{r}_{exit} = x_{exit}\mathbf{e}_x + y_{exit}\mathbf{e}_y + T_z\mathbf{n}_z. \tag{48}$$

Further, in reference to Fig. 1, the following equation is obtained:

$$\overrightarrow{\mathrm{P}_1''\mathrm{La}_0} = \Delta k_x \mathbf{e}_x + \Delta k_y \mathbf{e}_y. \tag{49}$$

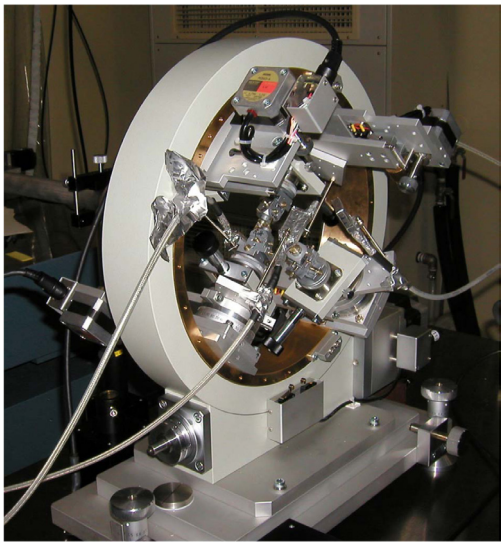

Figure 5: Photograph of the 'rotating four-quadrant phase retarder system' (reproduction of Fig. 3 (*b*) in Okitsu *et al.* (2012) [29]).

The X-ray amplitude $D_j^{(m)}(x_{exit}, y_{exit})$ to be calculated by using the fast Fourier transform (FFT) modulates the wave of $\exp\big(-\mathrm{i}2\pi\ \overrightarrow{\mathrm{La_0H}_j}\cdot\mathbf{r}\big)\ \mathbf{e}_j^{(m)}$. Considering that this amplitude is the coherent superposition of $\mathcal{D}_j^{(m)}(\Delta\mathbf{k})$, the next equation can be obtained:

$$
\begin{aligned}
&D_j^{(m)}(x_{exit}, y_{exit})\exp\big(-\mathrm{i}2\pi\overrightarrow{\mathrm{La_0H}_j}\cdot\mathbf{r}_{exit}\big)\\
&\quad=\int_{\Delta\mathbf{k}}^{D.S.}\mathcal{D}_j^{(m)}(\Delta\mathbf{k})\exp\big[-\mathrm{i}2\pi\big(\overrightarrow{\mathrm{P}_1'\mathrm{P}_1''}+\overrightarrow{\mathrm{P}_1''\mathrm{La_0}}\big)\cdot\mathbf{r}_{exit}\big]\exp\big(-\mathrm{i}2\pi\overrightarrow{\mathrm{La_0H}_j}\cdot\mathbf{r}_{exit}\big)\mathrm{d}S. \qquad (50)
\end{aligned}
$$

Here, let $\mathcal{D}_j'^{(m)}(\Delta k_x, \Delta k_y)$ be as follows:

$$
\mathcal{D}_j'^{(m)}(\Delta k_x, \Delta k_y)=\sum_{k=1}^{2n}\alpha_k^{(l)}\mathscr{D}_{j,k}^{(m)}(\Delta\mathbf{k})\exp\big(-\mathrm{i}2\pi\xi_k'''T_z\big), \qquad (51)
$$

$$
\text{where, } \overrightarrow{\mathrm{P}_{1,k}'\mathrm{P}_1''}=\xi_k'''\mathbf{n}_z.
$$

$\sum_{k=1}^{2n}$ in (51) has been obtained by extracting from the integration in the right side of (50). By substituting (51) into (50) and considering (48) and (49), the following equations can be obtained:

$$
\begin{aligned}
&D_j^{(m)}(x_{exit}, y_{exit})\\
&\quad=\int_{\Delta\mathbf{k}}^{D.S.}\sum_{k=1}^{2n}\alpha_k^{(l)}\mathscr{D}_{j,k}^{(m)}(\Delta\mathbf{k})\exp\big(-\mathrm{i}2\pi\xi_k'''T_z\big)\exp\big(-\mathrm{i}2\pi\overrightarrow{P_1''La_0}\cdot\mathbf{r}_{exit}\big)\mathrm{d}S \qquad (52a)\\
&\quad=\int_{\Delta k_x}\int_{\Delta k_y}\mathcal{D}_j'^{(m)}(\Delta k_x, \Delta k_y)\exp\big[-\mathrm{i}2\pi\big(\Delta k_x x_{exit}+\Delta k_y y_{exit}\big)\big]\mathrm{d}\Delta k_y\mathrm{d}\Delta k_x. \qquad (52b)
\end{aligned}
$$

The above equation (52) is a standard two-dimensional Fourier transform. The X-ray amplitude $D_j^{(m)}(x_{exit}, y_{exit})$ can be obtained by fast Fourier-transforming $\mathcal{D}_j'^{(m)}(\Delta k_x, \Delta k_y)$ defined by (51).

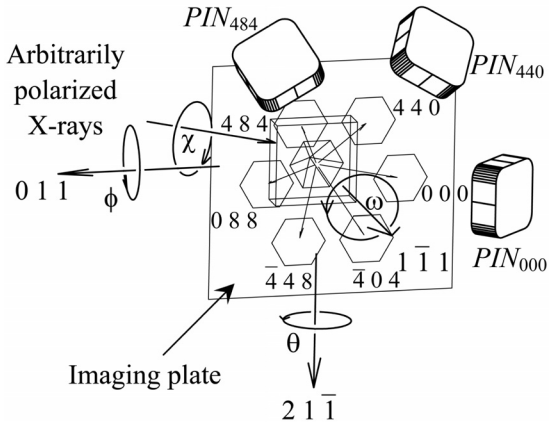

Figure 6: A schematic drawing of the goniometer on which the sample crystal was mount (reproduction of Fig. 7 in Okitsu *et al.* (2006)) [27]].

4 Experimental

4.1 Phase retarder system

The experiments to obtain 4-, 5-, 6- and 8-beam X-ray pinhole topographs were performed at BL09XU of SPring-8 by using the synchrotron X-rays. They were monochromatized to 18.245 keV by using the water-cooled diamond monochromator. The polarization state of the incident X-rays was controlled by using 'the rotating four-quadrant phase-retarder system' [27,29]. There were previous states before developing this polarization control system i.e. 'the two-quadrant X-ray phase retarder system' to compensate for the off-axis aberration [39] and 'the four-quadrant X-ray phase retarder system' to compensate for both the off-axis and chromatic aberrations [40]. These were invented, designed and manufactured by the present author. The experimental estimations were performed by the present author and Ueji to obtain the excellent results at the Photon Factory of KEK. These systems were further improved as shown in Figs. 4 and 5 such as to rotate around the optical axis to generate arbitrary polarized X-rays.

The transmission-type phase retarder [41–48] was innovative polarization-controll system. This can generate uniform phase shift between σ- and π-polarized X-rays compared with the reflection-type phase retarders [49–53]. Nevertheless, there was a problem of inhomogeneity (aberrations) of the phase shift owing to the angular divergence and energy spread of the incident X-rays. However, further homogeneous value of phase shift can be obtained by overlapping the phase retarder crystals such that the planes of incidence of them are inclined by 45° and 225° from the horizontal plane (two-quadrant system) [39] and by 45°, 135°, 225° and 315° (four-quadrant system) [40]. The two- and four-quadrant phase retarder system are particularly effective in the high energy region since the large value of total thickness of the diamond crystals can decrease the residual ununiformity of phase shift for σ- and π-polarized X-rays.

Fig. 4 is a schematic drawing of the phase retarder system. Fig. 5 is its photograph. This system consists of PR_n $\left(n \in \{1,2,3,4\}\right)$. These are [1 0 0]-oriented diamond crystals whose thickness are 1.545, 2.198, 1.565 and 2.633 mm and used in the vicinity of the angles to give 1 1 1 reflection in an asymmetric Laue geometry. How to control this system has been described in detail in the paper published in 2006 by the present author and his coauthors [27].

In the three-, 12- and 18-beam pinhole topograph experiments, the horizontally polarized

monochromatized synchrotron X-rays were incident on the crystal without using the phase retarder system. The photon energy for the three-beam case was 18.245 keV. That for 12- and 18-beam cases was 22.0 keV.

4.2 Silicon crystals uses as sample crystals and their position angle adjustment

Fig. 6 was reproduction of Fig. 7 in the paper published by the present author and his coauthors in 2006 [27]. The sample crystals used in the n-beam pinhole topograph experiment for $n \in \{3, 4, 5, 6, 8, 12, 18\}$ were [1 $\overline{1}$ 1]-oriented floating zone silicon crystals with high purity and high resistance. The thicknesses of the sample crystals were 10.0 mm in 12- and 18-beam cases and 9.6 mm in the other cases. The sample crystals were mounted on a goniometer that has four axes of χ, ϕ, ω and θ. Their angles were controlled as shown in Fig. 6. 0 0 0-forward diffracted and two reflected beam intensities were monitored with PIN photodiodes. The angles of the goniometer were controlled such that their intensities have maximum value. The positions of the diodes were adjusted such that the laser beam is incident on the detector. Before that, the rotation angles of the axes of the goniometer were calculated such as to reflect the laser beam in the beam direction of the reflected X-rays. It is impossible to adjust the positions of the diodes whose detection area was 15×15 mm such that the reflected X-rays were incident on them.

The dimension of the incident X-ray beam was set to be $25 \times 25 \mu$m with a four-quadrant slit system placed upstream of the phase retarder system. N pinhole topograph images of forward diffracted and reflected X-rays were simultaneously taken on the imaging plate set behind the sample crystal.

5 Results of the experiment and computer-simulation

5.1 Three-beam case

Figs. 7 [$E(a)$] and 7 [$S(a)$] are the experimentally obtained and computer-simulated images of 0 0 0-forward-diffracted, 0 4 4-reflected and $\overline{4}$ 0 4-reflected X-ray topographs [29]. Figs. 7 [$E(b)$] and 7 [$S(b)$] are enlargements of 0 4 4-reflected X-ray images of Figs. 7 [$E(a)$] and 7 [$S(a)$] Fine fringe regions ($FFR(1)$), ($FFR(2)$) and Y-shaped bright region (YBR) indicated by arrows in Fig. 7 [$S(b)$] are found also in Fig. 7 [$E(b)$], which shows the excellent agreement between the computer-simulated and experimentally obtained results.

5.2 Four-beam case

Figs. 8 [$E(x)$], 8 [$S(x)$] ($x \in \{a, b, c\}$) are experimentally obtained and computer-simulated images of 0 0 0-forward diffracted, $\overline{6}$ $\overline{2}$ 4-, $\overline{6}$ 2 8- and $\overline{6}$ 2 8-reflected X-rays. (a), (b) and (c) are different from each other in polarization state of the incident X-rays. These were obtained for (a): $+45°$-inclined linear polarization, (b): $-45°$-inclined linear polarization and (c): right-screwed circular polarization when viewed from the downstream direction.

Figs. 9 [$E(x)$] and 9 [$S(x)$] ($x \in \{a, b, c\}$) are enlargement of $\overline{6}$ 2 8-reflected X-ray images in Figs. 8 [$E(x)$] and 8 [$S(x)$] [29]. Fine Fringe Region ($FFR(1)$) can be found both in Figs. 9 [$E(a)$] and 9 [$S(a)$]. Fine Fringe Region ($FFR(2)$) can be found both in Figs. 9 [$E(x)$] and 9 [$S(x)$] ($x \in \{a, b, c\}$). Sharp lines [Knife Edge Line (KEL)] are found in all figures. These lines found in Figs. 9 [$E(a)$] and 9 [$S(a)$] are dark in comparison with Figs. 9 [$E(b)$] and 9 [$S(b)$]. In the cases of Figs. 9 [$E(c)$] and 9 [$S(c)$] intensities of these lines are intermediate between the

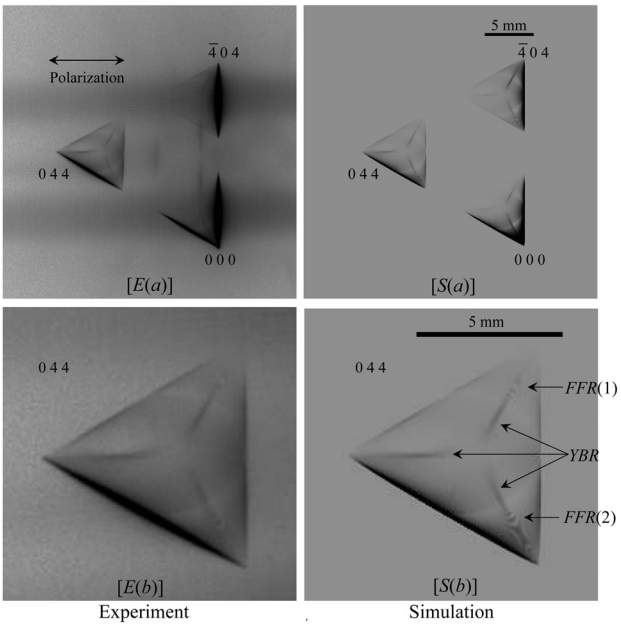

Figure 7: $[E(a)]$ and $[S(a)]$ are experimentally obtained and computer-simulated three-beam X-ray pinhole topographs with an incidence of horizontal-linearly polarized X-rays whose photon energy was 18.245 keV. $[E(b)]$ and $[S(b)]$ are 0 4 4 reflected X-ray images enlarged from $[E(a)]$ and $[S(a)]$, respectively (reproduction of Fig. 5 in Okitsu *et al.* (2012) [29]).

cases of (a) and (b). [Pattern like Fish Born (PFB)], [Arched Line (AL)] and [Bright Region (BR)] are not found in Figs. 9 $[E(a)]$ and 9 $[S(a)]$. However, they are found in the cases of $[E(b)]$, $[S(b)]$, $[E(c)]$ and $[S(c)]$ It has been clarified that the computer-simulated and experimentally obtained pinhole topograph images coincide with each other when the polarization state used in the experiment or assumed in the computer simulation agreed with each other.

Intensity ratio between the horizontally and vertically polarized X-rays is the same for (a), (b) and (c). However, there are difference in phase between the amplitudes of horizontally and vertically polarized X-rays. This difference in phase caused to the distinct difference in the topograph images.

Figs. 10 (a), 10 (b) and 10 (c) are rocking curves of the forward-diffracted X-ray intensity calculated based on the E-L theory under the assumptions of different polarization states of the incident X-rays:, (a) $+45°$ and (b) $-45°$-inclined linear polarization and (c) right-screwed circular polarization.

$\Delta\omega$ and $\Delta\phi$ are angular deviations around axes of $[\bar{2}\ \bar{1}\ 1]$ and $[0\ 1\ 1]$ directions, respectively, from the exact four-beam condition. Enhancement of the X-ray intensities are found at regions indicated to be '$\bar{6}\ \bar{2}\ 4$', '$\bar{6}\ 2\ 8$' and '0 6 6'. These were caused by the Borrmann effect (amorous transmission) [54]. Where these enhanced regions cross with each other to satisfy the four-beam condition, further enhancement of the forward-diffracted intensities owing to super Borrmann effect [55]. The enhancement of '$\bar{6}\ 2\ 8$' found in Fig. 10 (a) is relatively small in comparison with that found in Fig. 10 (b). In Fig. 10 (c), the situation is intermediate between them. The Bragg angle of $\bar{6}\ 2\ 8$ reflection for X-rays of 18.245 keV is 39.64°. Then, the polarization factor for π polarization $[\cos(2 \times 39.64°)]$ is calculated to be 0.186 that is a relatively small value

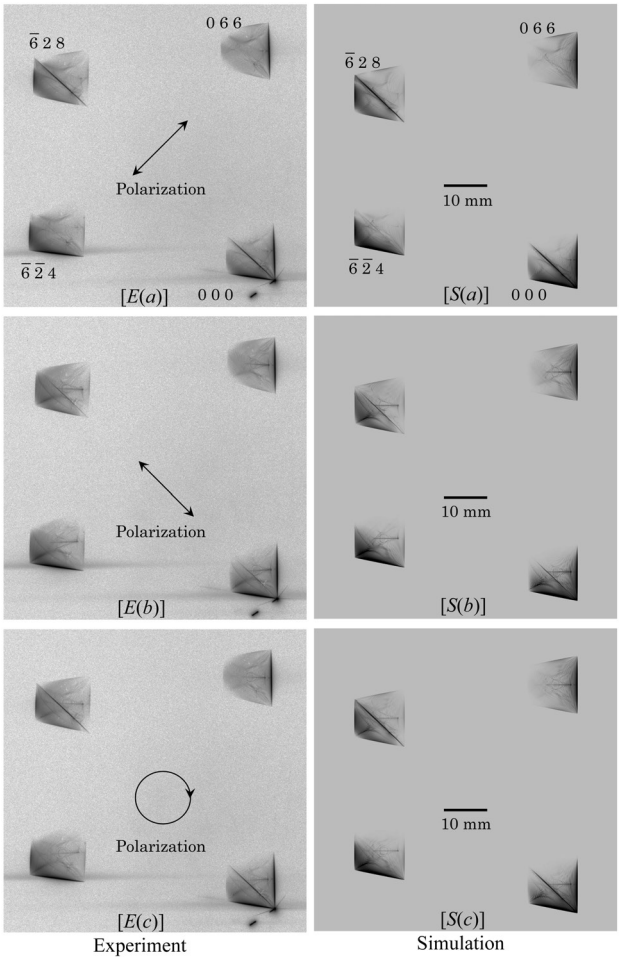

Figure 8: $[E(x)]$ and $[S(x)]$ ($x \in \{a, b, c\}$) are experimentally obtained and computer-simulated four-beam X-ray pinhole topographs with an incidence of $+45°$-inclined-linearly, $-45°$-inclined-linearly and right-screwed-circularly polarized X-rays whose photon energy was 18.245 keV (reproduction of Fig. 6 in Okitsu *et al.* (2012) [29]).

in comparison with that for σ polarization. Then, $-45°$-inclined linear polarization for $\overline{6}$ 2 8 reflection is almost π polarization, from which the relatively small enhancement of $\overline{6}$ 2 8 can be explained. The intensity of KEL depends on the polarization state of the incident X-rays for the same reason.

5.3 Five-beam case

There are cases in which five reciprocal lattice nodes simultaneously exist on a circle in the reciprocal space as shown in Fig. 1 of the paper published by the present author and his coauthors [27]. Fig. 11 $[E(a)]$ and 11 $[S(a)]$ are experimentally obtained and computer-simulated five-beam pinhole topographs. The vertical-linearly polarized X-rays that were converted from the horizontal-linearly polarized synchrotron X-rays. Figs. 11 $[E(b)]$ and 11 $[S(b)]$ are enlargements of $\overline{5}$ 5 5-reflected images [29]. [Knife Edge Line ($KEL(1)$, $KEL(2)$)] and [Harp-Shaped Patten ($HpSP$)] can be found both in the experimentally obtained and computer-simulated images.

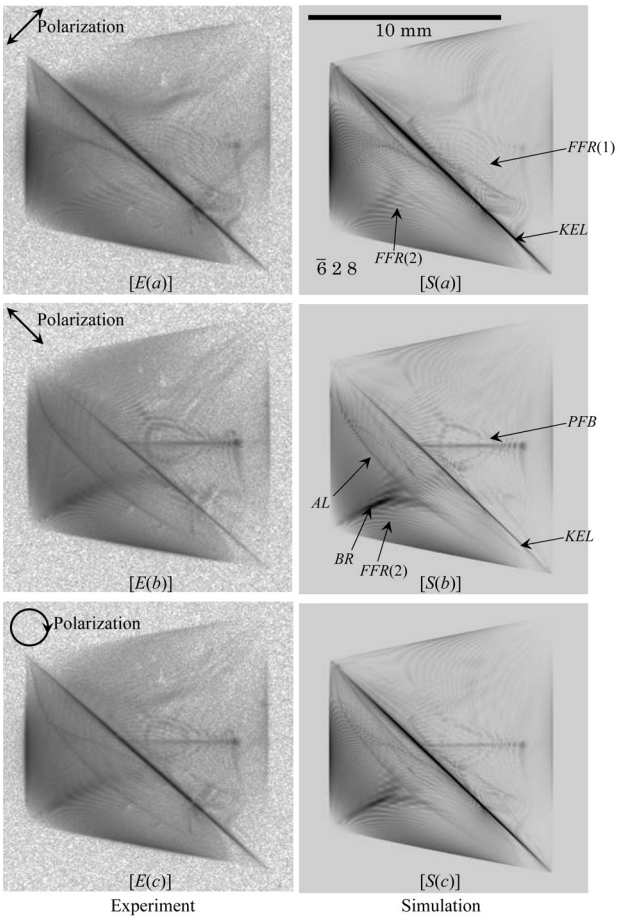

Figure 9: $[E(x)]$ and $[S(x)]$ ($x \in \{a, b, c\}$) are enlargements of $\overline{6}$ 2 8 reflected X-ray images in Fig. 8 $[E(x)]$ and $[S(x)]$ (reproduction of Fig. 7 in Okitsu *et al.* (2012)) [29]].

The directions of $KEL(1)$ and $KEL(2)$ found in Figs. 11 $[E(b)]$ and 11 $[S(b)]$ are parallel to the direction to tie the topograph images of $\overline{5}$ 5 5- and 3 3 3-reflected X-rays. This suggests the energy exchange between $\overline{5}$ 5 5-reflected and 0 0 0-forward diffracted X-rays and between $\overline{5}$ 5 5- and 3 3 3-reflected X-rays. Similar [Knife Edge Line (KEL)] can be found also in three-, four-, six- and eight-beam topographs.

5.4 Six-beam case

In the six-beam case reported by the present author and his coauthors [26–28], the topograph images were regular hexagons. However, in the six-beam case described in the present section, the topograph images are not regular hexagons.

Fig. 12 shows experimentally obtained and computer-simulated topographs with the incidence of horizontally polarized X-rays used in the experiment and assumed in the computer simulation [29]. Figs. Figs. 12 $[E(b)]$ and 12 $[S(b)]$ are enlargements of topographs of 0 6 6- and 2 6 4-reflected X-rays in Figs. 12 $[E(a)]$ and 12 $[S(a)]$. [Knife Edge Line ($KEL(1)$) and ($KEL(2)$)] and [Hart-Shaped Pattern (HSP)] can be found both in images experimentally obtained and computer-simulated.

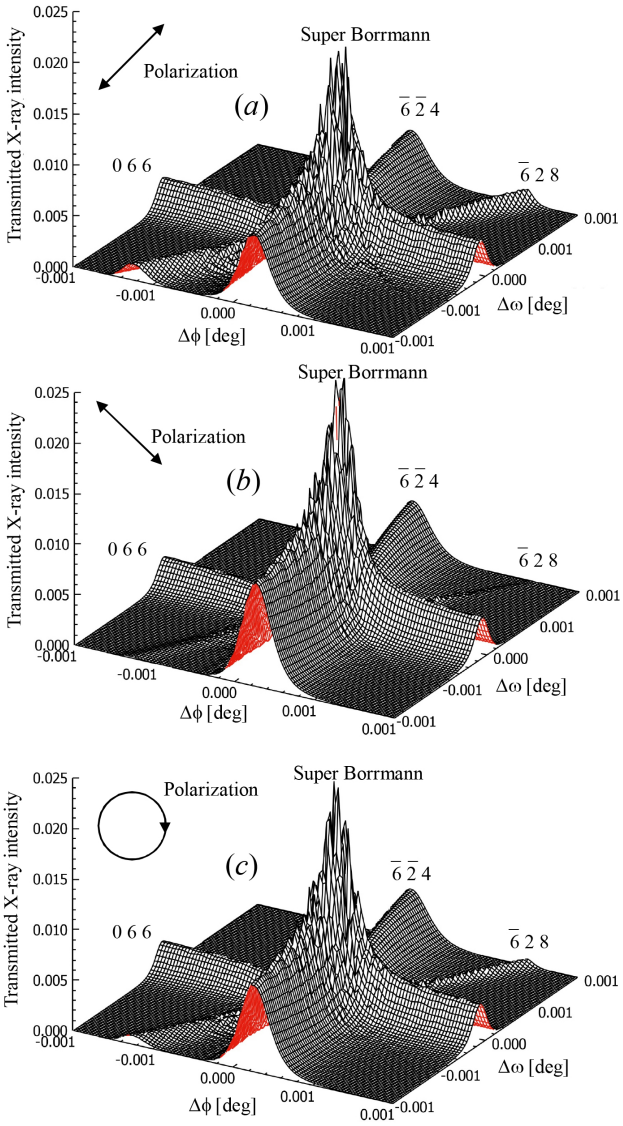

Figure 10: Transmittance of X-rays around the condition that $\overline{6}$ $\overline{2}$ 4-, $\overline{6}$ 2 8- and 0 6 6-reflected X-rays all in Laue geometries are simultaneously strong. $\Delta\omega$ and $\Delta\phi$ are angular deviations around [$\overline{2}$ $\overline{1}$ 1] and [0 1 1] axes from the exact four-beam condition.

In the cases of six-beam pinhole topographs whose shapes are regular hexagons, circular patterns that suggest the existence of cone-shaped path of energy flow. However, such circular patterns cannot be found in Fig. 12.

5.5 Eight-beam case

Fig. 13 shows eight-beam pinhole topographs whose reflection indices are as shown in Fig. 13 [S_h(T-T)] [29, 35].

Fig. 13 [E_x] ($x \in \{h, v\}$) show the experimentally obtained pinhole topographs obtained with the incidence of horizontally polarized ($x = h$) and vertically polarized ($x = v$) X-rays [29, 35].

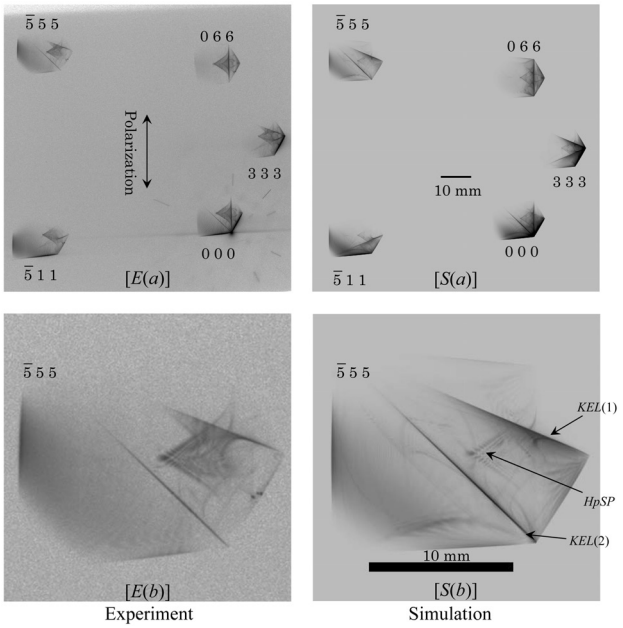

Figure 11: $[E(a)]$ and $[S(a)]$ are experimentally obtained and computer-simulated five-beam X-ray pinhole topographs with an incidence of vertical-linearly polarized X-rays whose photon energy was 18.245 keV. $[E(b)]$ and $[S(b)]$ are $\overline{5}$ 5 5 reflected X-ray images enlarged from $[E(a)]$ and $[S(a)]$ (reproduction of Fig. 8 in Okitsu *et al.* (2012) [29]).

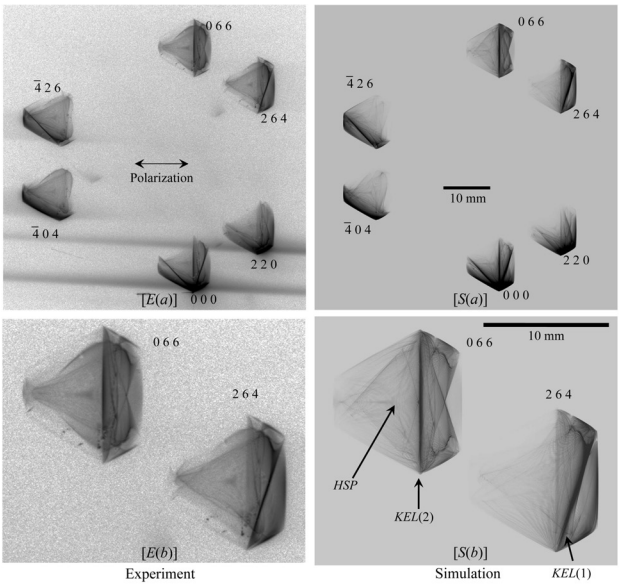

Figure 12: $[E(a)]$ and $[S(a)]$ are experimentally obtained and computer-simulated six-beam X-ray pinhole topographs with an incidence of horizontal-linearly polarized X-rays with a photon energy of 18.245 keV. $[E(b)]$ and $[S(b)]$ are 0 6 6 and 2 6 4 reflected X-ray images enlarged from $[E(a)]$ and $[S(a)]$ (reproduction of Fig. 9 in Okitsu *et al.* (2012)) [29]].

The horizontally polarized X-rays were obtained not by removing the phase-retarder crystals from the X-ray path but by reversing the sign of phase shift given by the diamond crystals that reflect the incident X-rays in the directions of the odd-numbered quadrant and the even-numbered quadrant directions.

Figs. 13 [S_x(T-T)] are computer-simulated pinhole topographs for the incidence of horizontally polarized ($x = h$) and vertically polarized X-rays obtained by solving the n-beam T-T equation (T-T simulation). However, Fig. 13 [S_x(E-L)] are obtained by fast Fourier-transforming the calculated X-ray amplitudes based on the E-L theory (E-L&FFT simulation). Fig. 15 (a) shows the geometrical relation of the crystal shape and the X-ray path. The E-L FFT simulation was performed under the assumption of geometry as shown in Figs. 15 (b) and 15 (c) at first. Then, after removing the parts of α_2 and β_2, the parts of (α_1) and (β_1) were calculated separately. Figs. 16 (α_1) and 16 (β_1) were linked to obtain Fig. 14 [S_v(E-L)]. The downward surface normal of the crystal in the cases of Figs. 15 (b) and 15 (c), are mutually perpendicular to each other. The important factor when considering the E-L&FFT simulation for such a complex geometry as shown in Fig. 15 (a), are that the plane waves consisting of the incident X-rays should be in phase at the incidence point on the crystal. Further, the distances of the incidence point of X-rays from the edge of the crystal should be strictly measured i.e. horizontally 16.5 mm and vertically 9.6 mm [see Figs. 15 (a), (b) and (c)]. Detail of the E-L&FFT simulation has been described in a paper published in 2019 [35].

Figs. 14 [S_x(T-T)], 14 [E_x] and 14 [S_x(E-L)] ($x \in \{h, v\}$) are enlargement of topograph images of 0 0 0-forward diffracted X-rays in Figs. 13 [S_x(T-T)], 13 [E_x] and 13 [S_x(E-L)], respectively.

In Fig. 14 [E_h] that was experimentally obtained, [Harp-Shaped Pattern ($HpSP$)], [Nail-Shaped Pattern (NSP)] and [Nail-Shaped Pattern (NSP)] are found. These patterns are found also in Figs. 14 [S_h(E-L)], and 14 [S_h(T-T)].

[Knife Edge Line (KEL)] as found in Fig. 14 [S_h(T-T)] is not found in Figs. 14 [E_h] and [S_h(E-L)]. When calculating [S_h(T-T)], Non-zero amplitude of incident X-rays only at the incidence point of X-rays was given as the boundary condition of Dirac's delta function. This bonday condition means the assumption that X-rays with infinite angular divergence are incident on the crystal. KEL is a sharp line that needs plane wave components whose directions of propagation are far different from the n-beam condition. This bondar condition is given in the computer simulation to obtain [S_h(T-T)]. However, the angular divergence of the incident X-rays practically used in the experiment to obtain the image of [E_h] is finite. When calculating [S_h(E-L)], the amplitude of the incident X-rays whose angular deviation from the exact n-beam condition is a finite range. This is considered to be the reason for that KEL is not observed in [E_h] and [S_h(E-L)].

Also in Figs. 14 [E_v], 14 [S_v(T-T)] and and 14 [S_v(E-L)], vertically polarized incident X-rays were used in the experiment or assumed in the simulation, $HpSP$ can be found. However, the intensity is weak in comparison with [S_h(T-T)], [E_h], and [S_h(E-L)].

In this eight-beam case, the time for the E-L&FFT simulation with parallel calculation using 24 cores was ∼8 minutes (about 100 times as fast as the T-T simulation). However, it cannot be concluded that the E-L&FFT is more excellent unconditionally as compared with the T-T simulation. The calculation time of the E-L&FFT simulation is constant not depending on the thickness of the crystal. On the other hand, that of the T-T simulation is proportional to the third power of the crystal thickness since the three-dimensional scanning in the Borrmann pyramid is need for the T-T simulation. Then, for the crystal whose thickness is 1.0 mm, the T-T simulation is 10 times as fast as compared with the E-L&FFT simulation.

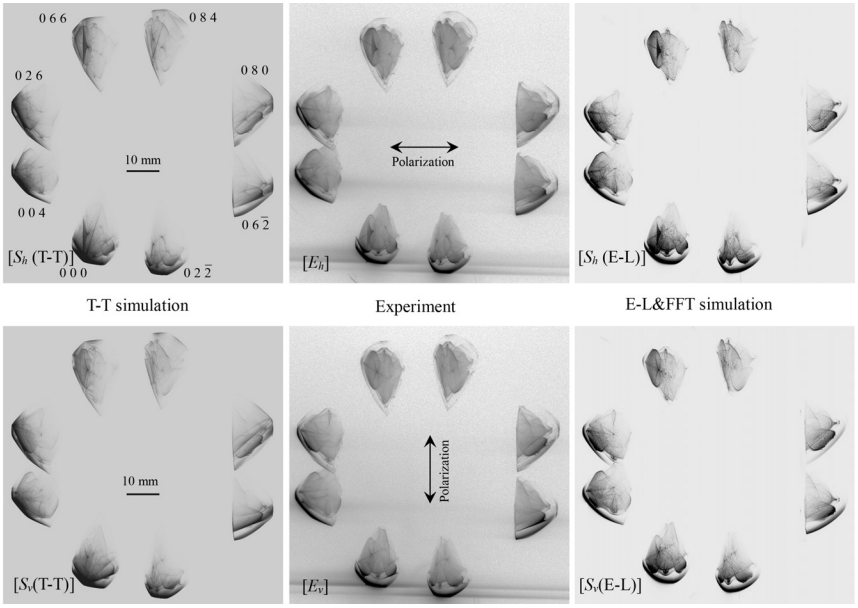

Figure 13: $[S_x(\text{T-T})]$, $[E_x]$, and $[S_x(\text{E-L})]$ ($x \in \{h, v\}$) are the T-T simulated, experimentally obtained and E-L&FFT simulated eight-beam pinhole topographs for horizontally ($x = h$) and vertically ($x = v$) polarized incident X-rays [reproduction of Fig. 5 in Okitsu *et al.* (2019)]

5.6 Twelve-beam case

The present author recognized that the largest number of reciprocal lattice nodes that exist on a circle in the reciprocal space is twelve for silicon crystal before publishing the present paper. On the other hand, he noticed that sixteen reciprocal lattice nodes exist on a circle in the reciprocal space. However, the sixteen-beam case is not described in the present paper.

Figs. 17 $[E(a)]$ and 17 $[S(a)]$ show twelve-beam pinhole topogpraphs experimentally obtained and computer-simulated based on the n-beam T-T equation [29]. The horizontally polarized synchrotron X-rays monochromatized to be 22.0 keV were directly incident on the silicon crystal. The indices of reflections are as shown in figures. Figs. 17 $[E(b)]$ and 17 $[S(b)]$ are enlargements of 2 4 2-reflected images in Figs. 17 $[E(a)]$ and 17 $[S(a)]$.

[Very Bright Region (VBR)], ['V-Shaped' Pattern (VSP)], [Central Circle (CC)] and ['U-Shaped' Pattern (USP)] in Fig. 17 $[S(b)]$ are also found in the experimentally obtained image in Fig. 17 $[E(b)]$.

5.7 18-beam case

Figs. 18 (a) and 18 (b) are 18-beam pinhole topographs experimentally obtained by using the synchrotron X-rays and E-L&FFT-computer-simulated [36]. Fig. 18 (a) were experimentally obtained by aiming to take six-beam pinhole topograph images with the synchrotron X-rays at 22.0 keV. However, around the six topograph images that were aimed to obtained, additional twelve images were found. After careful consideration concerning the geometry in the reciprocal space, further twelve reciprocal lattice nodes were found in the vicinity of the surface of the Ewald sphere. The arrangement of 18 ($= 6 + 12$) reciprocal lattice nodes can be drawn as shown in Fig. 19. In reference to this figure, The distances of H_i ($i \in \{0, 1, 2, 3, 4, 5\}$) and that of H_j ($j \in \{6, 7, \cdots, 17\}$) from the Laue Point La_0 are not the same. Therefore, dynamic change of

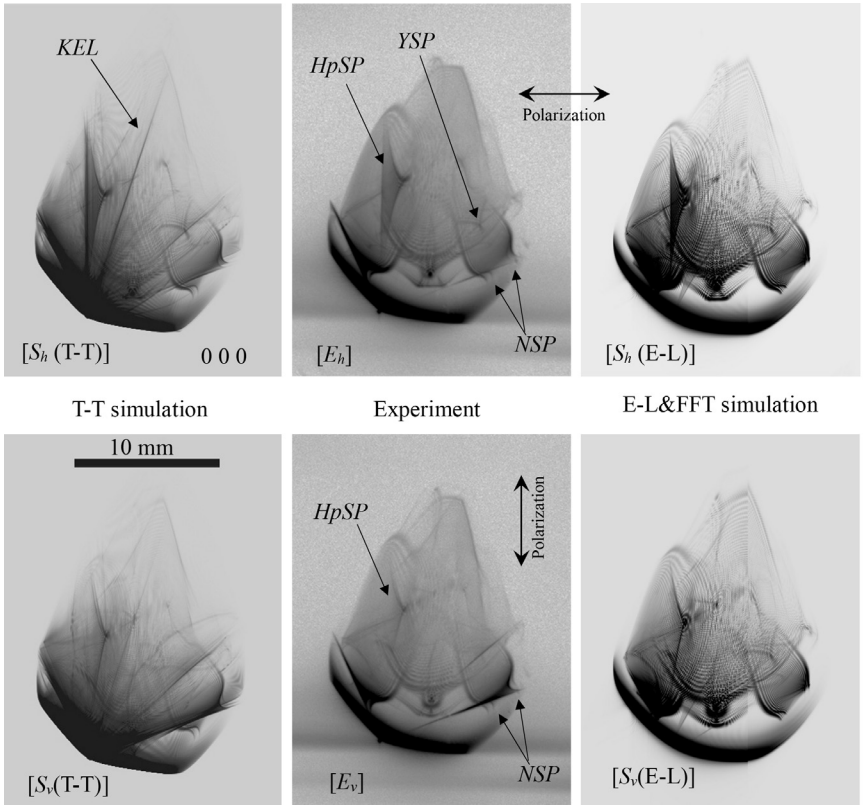

Figure 14: Enlargements of the 0 0 0 forward-diffracted images in Fig. 13 (reproduction of Fig. 6 in Okitsu *et al.* (2019)) [35]].

the 18-beam topograph images were found by changing slightly the photon energy. When the photon energy was assumed to be 21.98415 keV, good agreement between the experimentally obtained and the E-L&FFT-simulated pinhole topograph images was found as shown in Fig. 18. To obtain the E-L&FFT-simulated pinhole topograph images, (17) can be solved with the procedure described in §3.2. Directly calculated based on (17) were X-ray amplitude profiles when rotating the crystal. Similarly in the eight-beam case, it should be considered that plain wave X-rays that consist of the incident X-rays with the wave front of the delta function are in phase at the incident point of the X-rays.

It is clear from the reference to Fig. 19 that the Borrmann pyramid as shown in Fig. 2 (*b*) cannot be defined for this 18-beam case. However, the T-T simulation is not completely ineffective. (40) can be applied to the n-beam case for plane-wave incidence. Difference equation (45) derived from (40) can be The amplitude profile calculated by solving (45) can be fast Fourier-transformed to obtain the n-beam topograph images used to simulate the n-beam case even when $n = 18$ like this (T-T&FFT simulation). Regarding this method, a separate paper is in preparation.

6 Concluding remarks

Fig. 20 is a glitch map (simultaneous reflection map) calculated for silicon 2 2 0 reflection. The abscissa is the photon energy (eV) of the X-rays. The ordinate (ψ) is the rotation angle of the

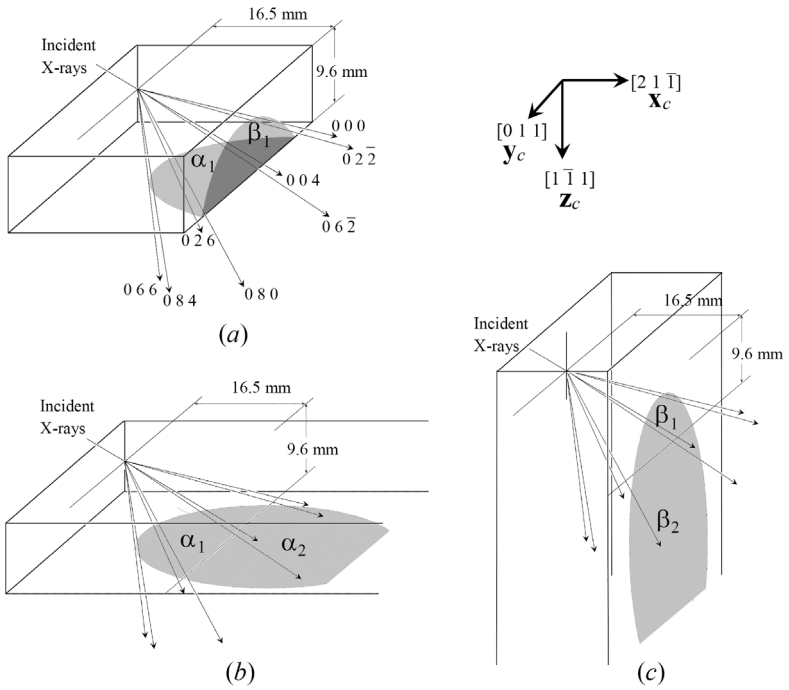

Figure 15: Geometry of the eight-beam pinhole topography. $\mathbf{x}_c$, $\mathbf{y}_c$, and $\mathbf{z}_c$ drawn on the upper right corner are unit vectors in the directions [2 1 $\overline{1}$], [0 1 1], and [1 $\overline{1}$ 1], respectively [reproduction of Fig. 1 in Okitsu *et al.* (2019)] [35].

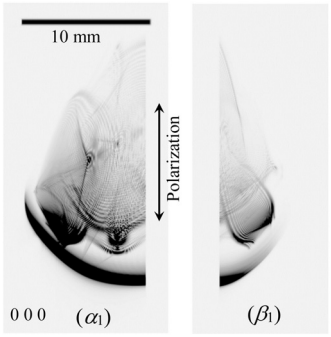

Figure 16: (α_1) and (β_1) are computed separately under the assumption of vertically polarized incident X-rays. These figures have been computed by projecting intensities of the 0 0 0 forward-diffracted X-rays on the exit planes α_1 and β_1 in Fig. 15 (a) on the imaging plate whose surface was normal to the [1 0 0] direction. X-ray intensities of α_2 and β_2 in Figs. 15 (b) and 15 (c) have been erased (reproduction of Fig. 8 in Okitsu *et al.* (2019) [35]).

crystal around [1 1 0] axis. $\psi = 0$ when $\mathbf{K}_{000} \times \mathbf{K}_{220}$ is parallel to the [0 0 1] direction. $\mathbf{K}_{000}$ and $\mathbf{K}_{220}$ are the wavevectors of 0 0 0-forward diffracted and 2 2 0-reflected X-rays. All red curves found in the glitches owing to the simultaneous reflections. These are caused by the reciprocal lattice nodes other than 2 2 0 existing simultaneously on the surface of the Ewald sphere to beak the two-beam condition.

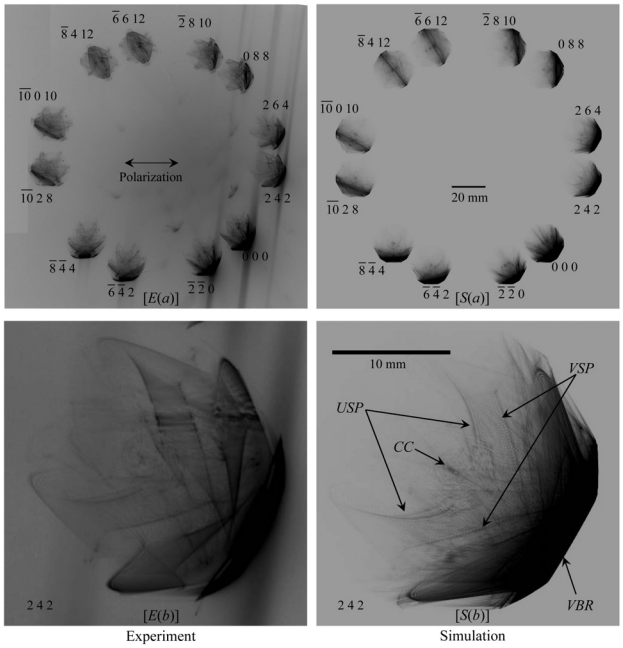

Figure 17: $[E(a)]$ and $[S(a)]$ are experimentally obtained and computer-simulated twelve-beam X-ray pinhole topographs with an incidence of horizontal-linearly polarized X-rays whose photon energy was 22.0 keV. $[E(b)]$ and $[S(b)]$ are 2 4 2 reflected X-ray images enlarged from $[E(a)]$ and $[S(a)]$ (reproduction of Fig. 12 in Okitsu *et al.* (2012) [29]).

The consideration on the glitches are important when designing such X-ray optical device as the monochromator, polarizer, analyzer and/or phase retarder. When scanning the photon energy e.g. by using the silicon 2 2 0 reflection, The two-beam approximation is broken at the photon energy where reciprocal lattice nodes whose indices are other than 2 2 0 exist on the surface of the Ewald sphere to cause the glitches (defects). In reference to Fig. 20, it can be found that the density of glitches is higher in the heigh-energy region compared with the low-energy region.

When an energy-scanning experiment is done by using the X-ray optical device, the value of ψ can be adjusted such that threre is no reciprocal lattice node causing the two-beam approximation in the vicinity of the surface of Ewald sphere In the energy ranges bellow 10 keV or so, such energy scan experiments are usually done by eliminating the glitches. However, it becomes difficult to eliminate the glitches whose density is proportional to the third power of the photon energy in the energy range higher than 20 keV. X-rays whose intensity is extremely high, are available at experimental stations of the third-generation synchrotron radiation sources. However, the X-ray optical devices cannot be designed only based on the two-beam dynamical diffraction theories in such a high energy range where the two-beam approximation is always broken. It is considered to be necessary to design the X-ray optical devices working in the high energy ranges based on the n-beam X-ray dynamical theories described by (19) and/or (34b). Simultaneously, advanced technique becomes necessary to control two or three axes e.g. θ and/or ψ of the goniometer on which the crystal devices are mount.

On the other hand, the n-beam effect cannot be ignored also when the two-beam approximation is always broken due to the large size of crystal lattice e.g. in the protein crystal structure analysis. Since the late 1980s, the use of two-dimensional detector generalized and are becoming

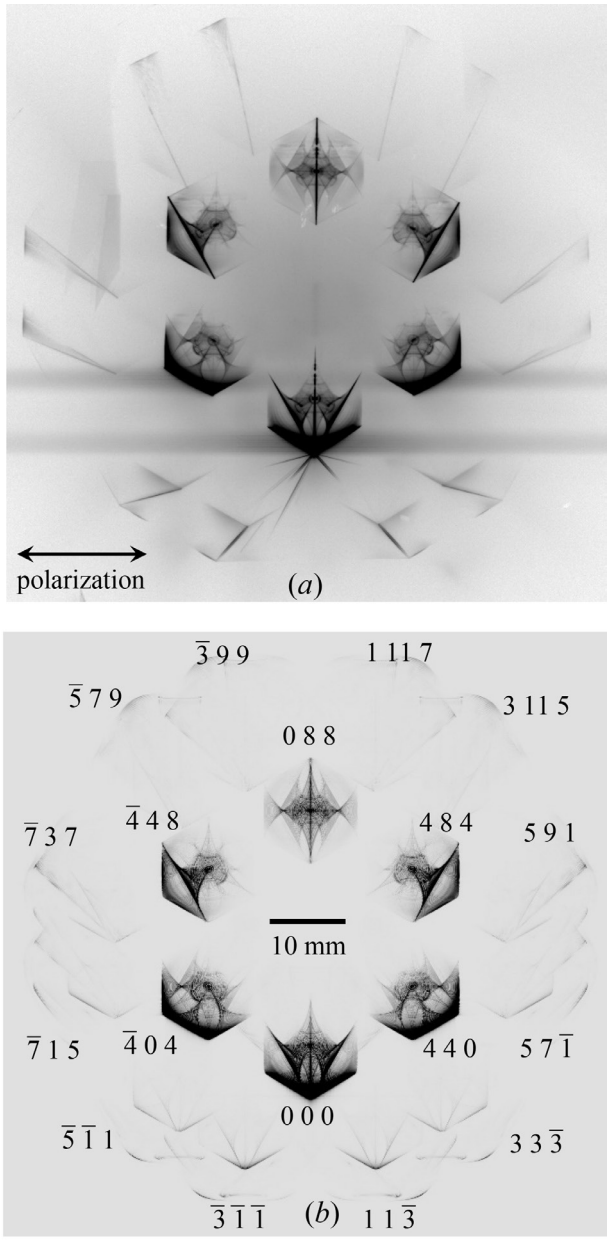

Figure 18: (a) Experimentally obtained and (b) E-L&FFT simulated 18-beam pinhole topographs. (b) was obtained by the E-L&FFT simulation under an assumption of an incidence of X-rays with a photon energy $E = 21.98415$ keV ($\Delta E = E - E_0 = -0.25$ eV, where $E_0 = 21.98440$ keV) (reproduction of Fig. 3 in Okitsu *et al.* (2019) [36]).

more sophisticated in the crystal structure analysis. Many diffraction spots; several dozen even in the cases of small molecular crystals and several hundred those are found in the cases of protein crystals, are simultaneously found in general. When seeing such situations, it is difficult to consider that the two-beam approximation is not broken. such cases where the two-beam approximation is broken even in the small molecular crystals, are well known as the Renninger effect [15]. In the case of protein crystals, it is rare that the reliability factor (R-factor) evalu-

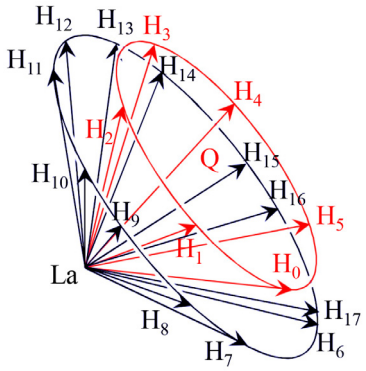

Figure 19: Six reciprocal lattice nodes are on a red (smaller) circle in reciprocal space. Outside of this circle, a black (larger) circle was observed on which twelve reciprocal lattice nodes were present. Q is the center of the red (smaller) circle (reproduction of Fig. 4 in Okitsu *et al.* (2019) [36]).

ated after the determination of the molecular structure is less than 10%. Even if the R-factor is evaluated to be 10%, it means the weighted discrepancy up to 20% between the X-ray diffraction intensities experimentally observed and calculated based on the kinematical theory from the determined molecular structure.

The present author has a hypothesis concerning the too large values of the R-factor for protein crystals that this problem is caused by the bankruptcy of the two-beam approximation due to the large density of reciprocal lattice nodes compared with the cases of small-molecule crystals. If the crystal structure factor $F_c(\mathbf{h})$ for h reflection were estimated by using the n-beam theory taking into account the reciprocal lattice nodes in the vicinity of the surface of the Ewald sphere to be compared with those measured by the experiment $F_o(\mathbf{h})$, the R-factor might be decreased dramatically. If that is the case for protein crystals, the crystal structures (and the phase problem) for protein crystals become to be solved by using the n-beam dynamical theory in place of the two-beam (kinematical) theory.

In Kato's book published in 1995, there is a description [in Japanese] as follows: When overviewing the history pf the X-ray diffraction in crystals, the backburn of the dynamical theory has been established by Darwin (1914) and by Ewald (1917) just after the discovery of the phenomenon of X-ray diffraction by von. Laue. The kinematical diffraction theory could be felt safe to use since its foundation has been given by their dynamical theories.

The present author had a lot of respect for Kato who passed away in 2002. However, he untouched almost at all the n-beam diffraction cases. In 1997, the present author asked him about the reason. He answered that he thought the solution of the dynamical theory cannot be obtained when Laue and Bragg geometries are mixed. However, the present author has already obtained the numerical solution of the T-T dynamical theory for a three-beam case when Laue and Bragg geometries were mixed. When telling him about this, he seemed to be confused.

Is it can be said that we cannot feel safe to use the kinematical theory based on the two-beam approximation when it is clarified to be broken ?

In 1949, Lipscomb suggested [56] that the phase information of the crystal structure factor can be extracted from the X-ray diffraction profile in principle. In the introduction of the famous article published by Collela in 1974 [22], the purpose of the study was to determine the phases of

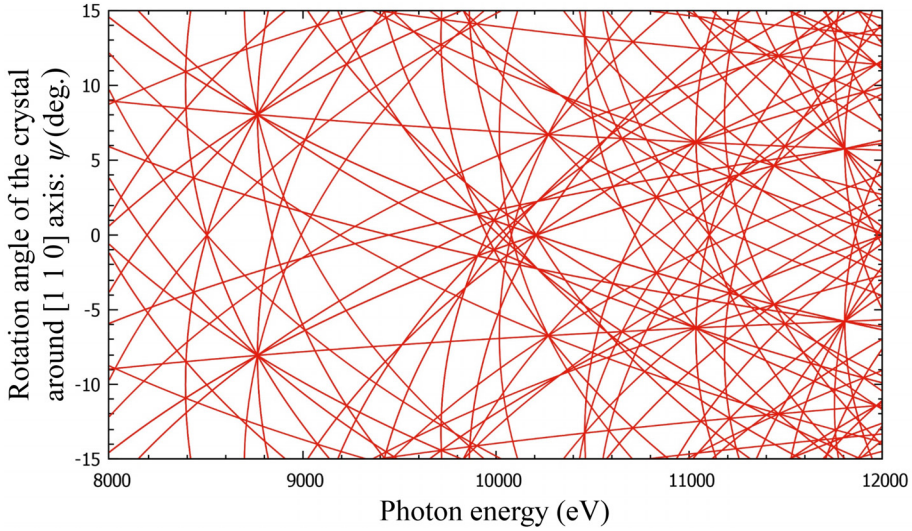

Figure 20: Glitch map (simultaneous reflection map) for silicon 2 2 0 reflection. ψ (the ordinate) is rotation angle (°) around [1 1 0] axis. The abscissa is X-ray photon energy (eV). ψ is *zero* when $\mathbf{K}_{000} \times \mathbf{K}_{220}$ is parallel to [0 0 1] direction. $\mathbf{K}_{000}$ and $\mathbf{K}_{220}$ are wave vectors of 0 0 0 transmitted and 2 2 0 reflected X-rays.

crystal structure factor by referring the Lipscomb's article. However, this has not been realized even today.

The phase problem in protein crystallography has been overcome mainly by using the heavy atom replacement and/or the method to replace methionine (one of the 20 amino acids included in molecules of the proteins) with selenomethionine that has selenium atom in place of sulfur [57] based on the two-beam approximation. The molecular replace methods are usually used when the similar or partial structures of the molecule have been determined by using the above-mentioned phasing methods. However, the phase determination of native protein crystals using the anomalous dispersion of sulfur is being surveyed due to its advantage without replacement.

When the molecular structures of protein crystals are obtained based on the n-beam theory in the future, the phases of the crystal structure factors might be determined only by indexing the diffraction spots simultaneously recorded on the two-dimensional detector.

It is impossible to realize the three-beam case for protein crystals whose density of reciprocal lattice nodes are extremely high. However, the n-beam Ewald-Laue (E-L) dynamical theory as described in (19) can deal with the cases where the n-reciprocal lattice nodes not on a circle exist in the vicinity of the surface of the Ewald sphere. The 18-beam pinhole topography is such a case. The 18 reciprocal lattice node not on a circle in the reciprocal space but exist in the vicinity of the surface of the Ewald sphere as shown in Fig. 19 has been computer-simulated and agreed well with the experimental result as shown in Fig. 18 (b). The n-beam T-T equation described as (34b) and/or (38) has been derived by Fourier-transforming the E-L theory (18) and/or (19). These can numerically be solved by taking into account the existence of all reciprocal lattice nodes in the vicinity of the surface of the Ewald sphere. The present author is now developing the computer program to solve the n-beam E-L theory described as (19) and n-beam T-T theory as (34b) and/or (35) for $n \sim 100$. It will be time-consuming.

The abilities of computers are rapidly being improved in all cases about calculation speed,

memory capacity and hard disk capacity The quantum computer may be realized in the future. These situations are important when considering the perspective of the n-beam theory. The present author will continue to study on the computer simulation of the n-beam X-ray diffraction with the equivalence in mind between the E-L and T-T dynamical theories.

Acknowledgement

The supercomputer system 'sumire', 'kashiwa' and 'sekirei' of the Institute for Solid State Physics, the University of Tokyo and 'TSUBAME 3.0' of Tokyo Institute of Technology were used for the computer simulations. The authors are indebted to Dr X.-W. Zhang of KEK Photon Factory, and Dr T. Oguchi of SPring-8 Service Corporation for their technical support in the present experiments and also to Professor Emeritus S. Kikuta of The University of Tokyo and Professor Emeritus H. Hashizume of Tokyo Institute of Technology for their encouragement and fruitful discussions regarding the present work.

The experimental part of the present work was conducted in cooperation with Dr. Y. Yoda and Dr. Y. Imai of SPring-8 JASRI and Dr. Y. Ueji of Rigaku Corporation.

Funding information

The theoretical component and the computer simulations of the present work were supported by the Nanotechnology Platform Project (No. 12024046) of the Ministry of Education, Culture, Sports, Science and Technology (MEXT), Japan.

The preliminary experiments were performed at BL4A and BL15C of Photon Factory and AR-NE3A of Photon Factory AR under the approval of the Photon Factory Program Advisory Committee (Proposal Nos. 97G-179, 97G-180, 99S2-003, 2003G202 and 2003G203). The main experiments were performed at BL09XU of SPring-8 under the approval of the Japan Synchrotron Radiation Research Institute (JASRI) (Proposal No. 2002A 0499-NMD3-np, 2003B 0594-NM-np, 2004A 0330-ND3c-np, 2004B 0575-ND3c-np, 2005B 0714 and 2009B 1384)

References

[1] Darwin, C. G. *Philos. Mag.* **27**, 315–333 (1914).

[2] Darwin, C. G. *Philos. Mag.* **27**, 675–690 (1914).

[3] Ewald, P. P. *Ann. Phys. 4. Folge* **54**, 519–597 (1917).

[4] Laue, M. v. *Ergeb. Exakten Naturwiss* **10**, 133–158 (1931).

[5] Zachariasen, W. H. *Theory of X-Ray Diffraction in Crystals* (J. Wiley & Sons, NewYork, 1945).

[6] Azároff, L. V. *et al. X-Ray Diffraction* (McGraw-Hill, 1974).

[7] Pinsker, Z. G. *Dynamical Scattering of X-Rays in Crystals* (Springer, 1978).

[8] Authier, A. *Dynamical Theory of X-Ray Diffraction, Reprinted with Revisions 2004, 2005.* (Oxford University Press, 2005).

[9] Takagi, S. *Acta Cryst.* **15**, 1311–1312 (1962).

[10] Takagi, S. *J. Phys. Soc. Jpn.* **26**, 1239–1253 (1969).

[11] Taupin, D. *Bull. Soc. Fr. Minéral. Cristallogr.* **87**, 469–511 (1964).

[12] Kato, N. *Z. Naturforsch* **28 a**, 604–609 (1973).

[13] Epelboin, Y. *Mater. Sci. Eng.* **73**, 1–43 (1985).

[14] Epelboin, Y. *Prog. Cryst. Growth Charact.* **14**, 465–506 (1987).

[15] Renninger, M. *Z. Phys.* **106**, 141–176 (1937).

[16] Saccocio, E. J. & Zajac, A. *Acta Cryst.* **18**, 478–480 (1965).

[17] Saccocio, E. J. & Zajac, A. *Phys. Rev. A* **139**, 255–265 (1965).

[18] Joko, T. & Fukuhara, A. *J. Phys. Soc. Jpn.* **22**, 597–604 (1967).

[19] Hildebrandt, G. *Phys. Stat. Sol.* **24**, 245–261 (1967).

[20] Ewald, P. P. & Héno, Y. *Acta Cryst.* **A24**, 5–15 (1968).

[21] Héno, Y. & Ewald, P. P. *Acta Cryst.* **A24**, 16–42 (1968).

[22] Colella, R. *Acta Cryst.* **A30**, 413–423 (1974).

[23] Thorkildsen, G. *Acta Cryst.* **A43**, 361–369 (1987).

[24] Larsen, H. B. & Thorkildsen, G. *Acta Cryst.* **A54**, 129–136 (1998).

[25] Okitsu, K. *Acta Cryst.* **A59**, 235–244 (2003).

[26] Okitsu, K., Imai, Y., Ueji, Y. & Yoda, Y. *Acta Cryst.* **A59**, 311–316 (2003).

[27] Okitsu, K. *et al. Acta Cryst.* **A62**, 237–247 (2006).

[28] Okitsu, K., Yoda, Y., Imai, Y. & Ueji, Y. *Acta Cryst.* **A67**, 550–556 (2011).

[29] Okitsu, K., Imai, Y. & Yoda, Y. *Recent Advances in Crystallography*, 67–86 (Intech open access publisher, 2012).

[30] Weckert, E. & Hümmer, K. *Acta Cryst.* **A53**, 108–143 (1997).

[31] Weckert, E. & Hümmer, K. *Cryst. Res. Technol.* **33**, 653–678 (1998).

[32] Colella, R. *Comments Cond. Mat. Phys.* **17**, 175–198 (1995).

[33] Colella, R. *Comments Cond. Mat. Phys.* **17**, 199–215 (1995).

[34] del Rio, M. S. & Dejus, R. J. *Proc. SPIE* **3448**, 340–345 (1998).

[35] Okitsu, K., Imai, Y., Yoda, Y. & Ueji, Y. *Acta Cryst.* **A75**, 474–482 (2019).

[36] Okitsu, K., Imai, Y. & Yoda, Y. *Acta Cryst.* **A75**, 482–488 (2019).

[37] Kohn, V. G. & Khikhlykha, D. R. *Acta Cryst.* **A72**, 349–356 (2016).

[38] Kohn, V. G. *Acta Cryst.* **A73**, 30–38 (2017).

[39] Okitsu, K., Ueji, Y., Sato, K. & Amemiya, Y. *J. Synchrotron Rad.* **8**, 33–37 (2001).

[40] Okitsu, K., Ueji, Y., Sato, K. & Amemiya, Y. *Acta Cryst.* **A58**, 146–154 (2002).

[41] Hirano, K., Izumi, K., Ishikawa, T., Annaka, S. & Kikuta, S. *Jpn. J. Appl. Phys.* **30**, L407–L410 (1991).

[42] Ishikawa, T., Hirano, K. & Kikuta, S. *J. Appl. Cryst.* **24**, 982–986 (1991).

[43] Hirano, K. *et al. Jpn. J. Appl. Phys.* **31**, L1209–L1211 (1992).

[44] Ishikawa, T., Hirano, K., Kanzaki, K. & Kikuta, S. *Rev. Sci. Instrum.* **63**, 1098–1103 (1992).

[45] Hirano, K., Ishikawa, T. & Kikuta, S. *Nucl. Instrum. Methods Phys. Res. A* **336**, 343–353 (1993).

[46] Hirano, K., Ishikawa, T. & Kikuta, S. *Rev. Sci. Instrum.* **66**, 1604–1609 (1995).

[47] Giles, C. *et al. J. Appl. Cryst.* **27**, 232–240 (1994).

[48] Giles, C. *et al. Nucl. Instr. Meth. A* **349**, 622–625 (1994).

[49] Hart, M. *Philos. Mag. B* **38**, 41–56 (1978).

[50] Annaka, S., Suzuki, T. & Onoue, K. *Acta Cryst.* **A36**, 151–152 (1980).

[51] Annaka, S. *J. Phys. Soc. Jpn.* **51**, 1927–1931 (1982).

[52] Golovchenko, J. A., Kincaid, B. M., Lvesque, R. A., Meixner, A. E. & Kaplan, D. R. *Phys. Rev. Lett.* **57**, 202–205 (1986).

[53] Mills, D. M. *Phys. Rev. B* **36**, 6178–6181 (1987).

[54] Borrmann, G. *Z. Phys.* **127**, 297–323 (1965).

[55] Borrmann, G. & Hartwig, W. *Z. Kryst.* **121**, 401–409 (1965).

[56] Lipscomb, W. N. *Acta Cryst.* **2**, 193–194 (1949).

[57] Hendrickson, W. A. *et al. Proc. Natl. Acad. Sci.* **86**, 2190–2194 (1989).